Daniel Christopher Haspinger, BSc

A Numerical Analysis of the Interrelation between Extracellular Smooth Muscle Orientation and the Intracellular Filament Overlap in Human Abdominal Aorta

MASTER'S THESIS

to achieve the university degree of

Diplom-Ingenieur

Master's degree programme: Biomedical Engineering

submitted to

Graz University of Technology

Supervisor

Univ.-Prof. Dipl.-Ing. Dr.techn. Gerhard A. Holzapfel

Institute of Biomechanics

Sae-Il Murtada, Ph.D., M.Sc. (Department of Biomedical Engineering, Yale University)
Justyna A. Niestrawska, M.Sc.RWTH (Institute of Biomechanics, Graz University of Technology)

Graz, November 2016

AFFIDAVIT

I declare that I have authored this thesis independently, that I have not used other than the declared sources/resources, and that I have explicitly indicated all material which has been quoted either literally or by content from the sources used. The text document uploaded to TUGRAZonline is identical to the present master‘s thesis.

Date

Signature

Inhaltsverzeichnis

Abstract **VII**

Zusammenfassung **IX**

Acknowledgement **XI**

1. Introduction **1**

2. Methods **3**
2.1. Continuum Mechanical Framework 3
2.1.1. Kinematics 3
2.1.2. Hyperelastic Stress Response 4
2.1.3. Elasticity Tensor 5
2.2. Constitutive Models 6
2.2.1. Constitutive Model of the Active Medial Smooth Muscle Cells . . 6
2.2.2. Layer Specific Constitutive Model for the Passive Arterial Wall . 12
2.3. Parameter Identification 13
2.4. Implementation into a Finite Element Program 14
2.5. Representative Finite Element Simulations 15
2.5.1. Uniaxial Isometric Contraction of an Aortic Medial Strip 15
2.5.2. Inflation and Contraction of an Arterial Ring 16

3. Results **17**
3.1. Parameter Identification 17
3.2. The Impact of Smooth Muscle Fiber Orientation and Filament Overlap Behavior on the Fitting of Active Material Parameters 18
3.3. Uniaxial Isometric Contraction of an Aortic Medial Strip – Validation of Model Implementation 20
3.4. Inflation and Contraction of an Arterial Ring 22

4. Discussion **27**

Bibliography **31**

Appendices **37**

A. Detailed Derivation of the Stress and Elasticity Tensors **39**

B. Analytical Expressions for Fitting **41**

C. Experimental Data Scaling **43**

Abstract

Vascular smooth muscle cells are one of the functional key constituents in the human abdominal aorta, located in the medial layer and forming two helices similar to collagen fibers. During development, angiogenesis and vascular remodeling, smooth muscle cells experience changes in their orientation and alignment as well as reorganization of their intracellular filament structure. In order to study the so far not so well-known interrelation between smooth muscle cell orientation and the intracellular filament structure in the human abdominal aorta a recently proposed chemo-mechanical coupled model was modified by introducing two families of muscle fibers and a non-symmetric filament overlap behavior, and implemented into a three-dimensional finite element framework. Active material parameters were obtained by fitting the model behavior to experimental data for different muscle fiber orientations. Fitting results highlighted that the non-symmetry of the filament overlap behavior depends on the muscle fiber orientation. Modifications of the smooth muscle fiber orientations and the intracellular filament structure, and their effects on the human abdominal aorta were investigated using a realistic finite element model of the aorta applying *in vivo* boundary conditions. We showed how changes in the arterial wall behavior due to alteration in smooth muscle fiber orientation can be reduced, and even prevented by adjusting the filament overlap behavior or the smooth muscle contractile unit density. Thus, modifying the intracellular filament structure or the smooth muscle cell content could be used as a therapeutic approach in response to pathological vascular adaptation processes where changes in smooth muscle fiber orientation is involved. But this would require further experimental and analytical studies.

Zusammenfassung

Glatte Muskelzellen sind mitunter einer der wichtigsten funktionellen Bestandteile der menschlichen Bauchaorta. In der Tunica Media gelegen formen sie zwei Helices ähnlich jener Struktur, wie sie Kollagenfasern vorweisen. Während der Gefäßentwicklung, Angiogenese und Remodellierung erfahren glatte Muskelzellen Veränderungen in ihrer Orientierung sowie eine strukturelle Umgestaltung ihrer intrazellulären Filamente. Um die bisher weitgehend unbekannten Wechselwirkungen zwischen der Orientierung der Muskelzellen und ihrer intrazellulären Struktur in der menschlichen abdominellen Aorta zu untersuchen, wurde ein kürzlich publiziertes chemo-mechanisch gekoppeltes Materialmodell modifiziert und in ein Finite Elemente Programm implementiert. Das Modell ermöglicht nun die Berücksichtigung zweier Muskelfaserfamilien, sowie ein unsymmetrisches Überlappungsverhalten der beteiligten Filamente. Zugehörige Materialparameter wurden aus experimentellen Daten für unterschiedliche vorgegebene Muskelfaserorientierungen bestimmt. Ergebnisse dieser Parameterbestimmung haben gezeigt, dass die Unsymmetrie des Überlappungsverhaltens von der Muskelfaserorientierung abhängig ist. Auswirkungen von Modifikationen der Muskelfaserorientierung sowie Veränderungen der intrazellulären Struktur auf die menschliche Bauchaorta wurden unter Verwendung eines realistischen Finite Elemente Modells der Aorta anhand von *in vivo* Randbedingungen numerisch untersucht. Es konnte gezeigt werden, dass Veränderungen im mechanischen Verhalten der Aortenwand, hervorgerufen durch eine Veränderung der Orientierung von Muskelzellen, kompensiert und unter Umständen sogar verhindert werden können. Dies kann durch eine entsprechende Anpassung des Überlappungsverhalten von beteiligten Filamenten bzw. durch eine Adaptierung der Dichte an kontraktilen Einheiten innerhalb einer Muskelzelle erfolgen. Eine herbeigeführte Modifikation der intrazellulären Struktur oder Muskelmasse könnte somit als ein möglicher therapeutischer Ansatz zur Reaktion auf pathologische Veränderungsprozesse von Gefäßen verwendet werden, in denen eine Umorientierung von glatten Muskelzellen involviert ist. Dies erfordert jedoch die Durchführung zahlreicher weiterer experimenteller als auch analytischer Untersuchungen.

Acknowledgement

Special thanks go to Prof. Gerhard Holzapfel who gave me the opportunity to get an insight into the interesting research field of biomechanics by employing me as a teaching and research assistant, and finally by supervising this thesis. I would also like to express my sincere and deep gratitude to Justyna Niestrawska and Sae-Il Murtada for their supervision and support during the whole time. I have learned a lot within these months and I generated my interest in this field of research, thank you very much!

Furthermore, I would like to thank my colleagues at the Institute of Biomechanics, especially Osman Gültekin and Kewei Li who always had a sympathetic ear for me – for the numerous discussions we led and the informative conversations we had.

I want to express my sincere gratitude to my girlfriend, Julia and all of my friends who supported me while finishing this thesis, who motivated me day by day, who ensured that I kept a clear brain, so that I could totally focus on writing this thesis.

Last but not least, I would like to thank my mother, Silvia, and my grandmother, Hermine, for your constant support in every sense and that you never stopped believing in me, and to my deceased father, Edmund, and my grandfather, Josef, your generous love, your trust, your encouragement, your endurance and your warmth will always be remembered and never forgotten.

Daniel Ch. Haspinger

1. Introduction

Vascular smooth muscle cells play a significant role in short-term as well as long-term changes of the human abdominal aorta (Cox, 1975; Li et al., 1998). During development, angiogenesis and vascular remodeling, smooth muscle cells experience changes in their orientation and alignment (Mantella et al., 2015). A time dependent reorganization of vascular smooth muscle cells perpendicular to the axis of the applied cyclic stretch during *in vitro* experiments has been reported (Chen et al., 2003; Standley et al., 2002) where the reorientation was dependent on the applied cyclic stretch frequency (Liu et al., 2008). *In vivo* experiments performed on basilar arteries of normotensive rats revealed an almost uniform circumferential alignment of vascular smooth muscle cells. In contrast, spontaneously hypertensive rats showed a significantly altered pattern of arrangement (distribution) and main orientation of contractile smooth muscle cells (Arribas et al., 1996). Numerous factors such as the frequency, direction and of course the amount of applied stretch have been shown to play a major role in the reorientation of vascular smooth muscle cells *in vivo* as well as *in vitro* (Mantella et al., 2015).

The healthy human abdominal aorta is a large elastic artery and consists of three distinct layers: tunica intima, tunica media and tunica adventitia. The tunica intima is the innermost layer of the abdominal aorta and composed of a single layer of endothelial cells. Endothelial cells are integrated into several important physiological processes such as regulating the exchange of substances between blood and the underlying cells, inhibition and activation of blood coagulation mechanisms (Butcher and Nerem, 2007) and most importantly production of important substances such as nitric oxide (NO) and endothelin-1 (ET-1) being responsible for the modulation of the vascular tone. The medial layer of the abdominal aorta (tunica media) is made up of 40 to 70 alternating layers of spindle-shaped smooth muscle cells and elastic lamellae, composed of the extra-cellular matrix proteins elastin, collagen (30% of type I and type III of 70%, Holzapfel et al. (2000)) and proteoglycans. The adventitia is the outermost layer of the arterial wall and comprises elastin, fibroblasts (responsible for elastin and collagen production) and thick bundles of wavy collagen fibrils which prevent the artery from overstretching and rupture at high blood pressure levels. Smooth muscle cells in the human abdominal aorta have been reported to be oriented symmetrically with a direction in the circumferential - axial plane forming of two fibrous helices in the medial layer (Holzapfel et al., 2002; Horný et al., 2010). Findings of Horný et al. (2010) suggest that the collagen fiber orientation and the orientation of smooth muscle nuclei correlate.

Smooth muscle cells are able to produce active tension over a large range of muscle lengths in the circumferential direction which can be described through a length-tension

relationship (Cox, 1975, 1978; Dobrin, 1973). This length-tension relationship, which also can be described as a stretch-active stress relationship, has been modeled previously (Carlson and Secomb, 2005; Gleason et al., 2008; Rachev and Hayashi, 1999; Zulliger et al., 2004), and described as a rearrangement of the intracellular filament structure, more specifically the filament overlap between the actin and myosin filaments (Murtada et al., 2012). The filament overlap set the maximal number of attached cross-bridges in an average contractile unit.

Smooth muscle cells are known to be able to adapt their length-tension behavior as a relatively quick response when being subjected to a sustained changed loading condition (Gunst et al., 2003; Herrera et al., 2005; Syyong et al., 2008; Wang et al., 2001; Yamin and Morgan, 2012). This adaption process is partly directed by a reorganization of the intracellular filaments such as the actin and myosin filaments affect the filament overlap (Gunst et al., 2003; Herrera et al., 2005; Yamin and Morgan, 2012) and the number of contractile units (Herrera et al., 2005). However, most filament overlap function studies have been conducted for smooth muscle cells aligned in the circumferential direction and no detailed analysis has been made investigating the relationship and link between the extracellular smooth muscle cell orientation and the intracellular filament structure. The relationship between the smooth muscle cell orientation and the intracellular filament structure has not yet been addressed and the effect and the role of their relationship is not well known. In the present study we address this structural connection ranging between different length-scales to better understand the role of smooth muscle contraction during vascular adaptation. We use a modified version of a chemo-mechanical coupled model proposed by Murtada et al. (2010a, 2012) and Stålhand et al. (2011) that we implement into a three-dimensional finite element framework. This framework is used to study how changes in the smooth muscle cell orientation and intracellular filament structure affect the active behavior in the human abdominal aorta.

2. Methods

2.1. Continuum Mechanical Framework

In this section the basic continuum mechanical relationships associated with the constitutive models of the arterial wall presented in this thesis are summarized. These are in particular the finite deformation kinematics, the hyperelastic stress response, and the elasticity tensor required for an implementation into a finite element program. The interested reader is referred to Ogden (1997) and Holzapfel (2000) for more detailed information.

2.1.1. Kinematics

At time t_0 we assume a solid body being in a load- and stress-free reference configuration $\Omega_0 \subset \mathbb{R}^3$. By means of the motion $\boldsymbol{\chi}_t$ a material point $\mathbf{X} \in \Omega_0$ can be transformed to a position $\mathbf{x} = \boldsymbol{\chi}_t(\mathbf{X})$ in the deformed (current, spatial) configuration, defined as $\Omega \subset \mathbb{R}^3$ at the current time t. In order to describe the deformation of a solid body the deformation gradient, defined as $\mathbf{F} = \partial \boldsymbol{\chi}_t(\mathbf{X}) / \partial \mathbf{X}$ is mainly used in continuum mechanics. According to the numerical issues reported in Flory (1961); Ogden (1978); Zienkiewicz and Taylor (2000) regarding incompressibility we consider a multiplicative decomposition of the deformation gradient into a volume-changing part $\mathbf{F}_{\text{vol}} = J^{1/3}\mathbf{I}$ and a volume-preserving part $\overline{\mathbf{F}} = J^{-1/3}\mathbf{F}$ so that $\mathbf{F} = \mathbf{F}_{\text{vol}}\overline{\mathbf{F}}$, where J is the volume ratio defined as $J(\mathbf{X}) = \det \mathbf{F} > 0$, and $\det \overline{\mathbf{F}} = 1$. Further, $\mathbf{C}$ and $\mathbf{b}$ are the right and left Cauchy-Green tensors, respectively, together with their corresponding unimodular counterparts $\overline{\mathbf{C}}$ and $\overline{\mathbf{b}}$, defined in terms of the deformation gradient as

$$\begin{aligned} \mathbf{C} &= \mathbf{F}^{\mathrm{T}}\mathbf{F} = J^{2/3}\overline{\mathbf{C}}, \qquad & \overline{\mathbf{C}} &= \overline{\mathbf{F}}^{\mathrm{T}}\overline{\mathbf{F}}, \\ \mathbf{b} &= \mathbf{F}\mathbf{F}^{\mathrm{T}} = J^{2/3}\overline{\mathbf{b}}, \qquad & \overline{\mathbf{b}} &= \overline{\mathbf{F}}\overline{\mathbf{F}}^{\mathrm{T}}. \end{aligned} \tag{2.1}$$

The three principal strain invariants I_i and the corresponding modified principal strain invariants $\bar{I}_i$, $i = 1, 2, 3$, can be defined in terms of the right Cauchy-Green tensor as

$$I_1 = \mathrm{tr}\mathbf{C} = \mathbf{C} : \mathbf{I} = J^{2/3}\bar{I}_1, \qquad \bar{I}_1 = \mathrm{tr}\overline{\mathbf{C}} = \overline{\mathbf{C}} : \mathbf{I}, \tag{2.2}$$

$$I_2 = \frac{1}{2}\left[{I_1}^2 - \mathrm{tr}\left(\mathbf{C}^2\right)\right] = J^{4/3}\bar{I}_2, \qquad \bar{I}_2 = \frac{1}{2}\left[{\bar{I}_1}^2 - \mathrm{tr}\left(\overline{\mathbf{C}}^2\right)\right], \tag{2.3}$$

and

$$I_3 = \det \mathbf{C} = \left(\det \mathbf{F}\right)^2, \qquad \bar{I}_3 = \det \overline{\mathbf{C}} = \left(\det \overline{\mathbf{F}}\right)^2 = 1. \tag{2.4}$$

Finally, let us assume the existence of a vector $\mathbf{M}$ defined in the reference configuration, with $|\mathbf{M}| = 1$. The motion $\boldsymbol{\chi}_t$ maps this vector into its current configuration, characterized by $\mathbf{m} = \mathbf{F}\mathbf{M}$, where $|\mathbf{m}|^2 = \lambda_{\mathrm{m}}^2 = I_{\mathrm{m}_4}$ denotes the square of the stretch in the direction $\mathbf{m}$, with the pseudo-invariant $I_{\mathrm{m}_4} = \mathbf{C} : \mathbf{M} \otimes \mathbf{M}$. The push-forward of $\mathbf{M}$ via the unimodular part of the deformation gradient $\overline{\mathbf{F}}$ gives the vector $\overline{\mathbf{m}} = \overline{\mathbf{F}}\mathbf{M}$, with the unimodular form of the pseudo-invariant, i.e. $\overline{I}_{\mathrm{m}_4} = \overline{\mathbf{C}} : \mathbf{M} \otimes \mathbf{M}$.

2.1.2. Hyperelastic Stress Response

In the context of finite hyperelasticity we assume the existence of a Helmholtz free-energy function Ψ, defined per unit reference volume, which we additively decompose into its volumetric (dilational) part $U(J)$ and isochoric (distortional) part $\overline{\Psi}(\overline{\mathbf{C}})$ as (Holzapfel, 2000)

$$\Psi = U(J) + \overline{\Psi}(\overline{\mathbf{C}}). \tag{2.5}$$

From the Clausius-Planck inequality (assuming a reversible isothermal process) and by applying the standard Coleman-Noll procedure, we receive the constitutive equation for the second Piola-Kirchhoff stress tensor as

$$\mathbf{S} = 2\frac{\partial \Psi(\mathbf{C})}{\partial \mathbf{C}} = \mathbf{S}_{\mathrm{vol}} + \overline{\mathbf{S}}, \tag{2.6}$$

using the volumetric-isochoric split from Eq. (2.5). The purely volumetric stress contribution of Eq. (2.6) is specified as

$$\mathbf{S}_{\mathrm{vol}} = 2\frac{\partial U(J)}{\partial \mathbf{C}} = 2\frac{\partial U(J)}{\partial J}\frac{\partial J}{\partial \mathbf{C}} = pJ\mathbf{C}^{-1}, \tag{2.7}$$

with the hydrostatic pressure $p(J) = \mathrm{d}U(J)/\mathrm{d}J$ and the derivative of J with respect to the symmetric tensor $\mathbf{C}$, which is $J\mathbf{C}^{-1}$. The purely isochoric part of Eq. (2.6) reads

$$\overline{\mathbf{S}} = 2\frac{\partial \overline{\Psi}(\overline{\mathbf{C}})}{\partial \mathbf{C}} = J^{-2/3}\mathbb{P} : 2\frac{\partial \overline{\Psi}(\overline{\mathbf{C}})}{\partial \overline{\mathbf{C}}} = J^{-2/3}\mathrm{Dev}\tilde{\mathbf{S}}, \tag{2.8}$$

where we define the fictitious isochoric contribution of the second Piola-Kirchhoff stress tensor as

$$\tilde{\mathbf{S}} = 2\frac{\partial \overline{\Psi}(\overline{\mathbf{C}})}{\partial \overline{\mathbf{C}}}, \tag{2.9}$$

and the fourth-order projection tensor with respect to the reference configuration as

$$\mathbb{P} = \mathbb{I} - \frac{1}{3}\mathbf{C}^{-1} \otimes \mathbf{C}. \tag{2.10}$$

A detailed derivation of Eqs. (2.7) and (2.8) can be found in the Appendix A.

2.1.3. Elasticity Tensor

In order to obtain results with reasonable accuracy for nonlinear problems in the field of computational finite elasticity an incremental or iterative solution method (of Newton's type) in combination with an adequate convergence criterion is required (Wriggers, 2008). Therefore, a consistent linearization of the constitutive equation is needed, which yields the so-called elasticity tensor. The material representation of the elasticity tensor can be obtained from the total differential $\mathrm{d}\mathbf{S} = \mathbb{C} : 1/2\ \mathrm{d}\mathbf{C}$, in which the symmetric fourth-order elasticity tensor in decoupled form is introduced as

$$\mathbb{C} = 2\frac{\partial \mathbf{S}(\mathbf{C})}{\partial \mathbf{C}} = 4\frac{\partial^2 \Psi(\mathbf{C})}{\partial \mathbf{C} \partial \mathbf{C}} = \mathbb{C}_{\mathrm{vol}} + \overline{\mathbb{C}}, \tag{2.11}$$

where we have used Eqs. (2.5) and (2.6). The purely volumetric contribution of the elasticity tensor in the Lagrangian description of Eq. (2.11) reads

$$\mathbb{C}_{\mathrm{vol}} = 2\frac{\partial \mathbf{S}_{\mathrm{vol}}(\mathbf{C})}{\partial \mathbf{C}} = 2\frac{\partial \left(pJ\mathbf{C}^{-1} \right)}{\partial \mathbf{C}} \tag{2.12}$$

$$= \left(pJ + J^2 \frac{\mathrm{d}p}{\mathrm{d}J} \right) \mathbf{C}^{-1} \otimes \mathbf{C}^{-1} - 2pJ\mathbf{C}^{-1} \odot \mathbf{C}^{-1}, \tag{2.13}$$

with $\mathrm{d}p/\mathrm{d}J = \mathrm{d}^2U(J)/\mathrm{d}J^2$. A comprehensive derivation of Eq. (2.12) as well as the definition of $\odot$ is given in Appendix A. The purely isochoric contribution of Eq. (2.11) is defined as (Holzapfel, 2000)

$$\overline{\mathbb{C}} = \mathbb{P} : \tilde{\mathbb{C}} : \mathbb{P}^{\mathrm{T}} + \frac{2}{3}\mathrm{Tr}\left(J^{-2/3}\tilde{\mathbf{S}} \right) \tilde{\mathbb{P}} - \frac{2}{3}\left(\mathbf{C}^{-1} \otimes \overline{\mathbf{S}} + \overline{\mathbf{S}} \otimes \mathbf{C}^{-1} \right), \tag{2.14}$$

where the fourth-order fictitious elasticity tensor in the material description is

$$\tilde{\mathbb{C}} = 4J^{-4/3}\frac{\partial^2 \overline{\Psi}(\overline{\mathbf{C}})}{\partial \overline{\mathbf{C}} \partial \overline{\mathbf{C}}}, \tag{2.15}$$

the modified Lagrangian projection tensor of fourth-order is

$$\tilde{\mathbb{P}} = \left(\mathbf{C}^{-1} \odot \mathbf{C}^{-1} \right) : \mathbb{P}^{\mathrm{T}} = \mathbf{C}^{-1} \odot \mathbf{C}^{-1} - \frac{1}{3}\mathbf{C}^{-1} \otimes \mathbf{C}^{-1}, \tag{2.16}$$

and the trace is $\mathrm{Tr}\,(\bullet) = (\bullet) : \mathbf{C}$, together with

$$\mathbb{P}^{\mathrm{T}} = \mathbb{I} - \frac{1}{3}\mathbf{C} \otimes \mathbf{C}^{-1}, \tag{2.17}$$

according to Eq. (2.10).

2.2. Constitutive Models

As already mentioned in the continuum mechanical framework and shown in Eq. (2.5), we assume a possible split of the free-energy function Ψ characterizing the arterial wall into two parts, a purely volumetric contribution, particularized as

$$U(J) = \frac{\kappa}{2}(\ln J)^2, \tag{2.18}$$

and a layer specific isochoric part $\overline{\Psi}$ which reflects the micro-structure and mechanical properties of the arterial wall. Note that $\kappa > 0$, denoting the bulk modulus, serves here as a penalty parameter, where an increase of κ reduces violation of the incompressibility constraint. In the limiting case $\kappa \to \infty$ the constraint is exactly enforced and the free-energy function Ψ represents a functional for an incompressible material with $J = 1$. For numerical reasons the penalty parameter is chosen to be $\kappa = 10^5$ kPa for all subsequent simulations.

Since it is only the medial layer of a healthy arterial wall that contains smooth muscle cells, we additively decompose the isochoric part $\overline{\Psi}$ of the free-energy function for the media into an active part considering smooth muscle contractility and into a passive contribution representing the structural and mechanical properties of passive components (ground matrix and collagen fibers), i.e. $\overline{\Psi} = \overline{\Psi}_{\mathrm{a}} + \overline{\Psi}_{\mathrm{p}}$. Hence, the isochoric part of the second Piola-Kirchhoff stress tensor $\overline{\mathbf{S}}$ and elasticity tensor in the material description $\overline{\mathbb{C}}$ together with their corresponding fictitious expressions denoted by $\tilde{\mathbf{S}}$ and $\tilde{\mathbb{C}}$ can also be split into an active and passive part, according to

$$\overline{\mathbf{S}} = \overline{\mathbf{S}}_{\mathrm{a}} + \overline{\mathbf{S}}_{\mathrm{p}}, \qquad \tilde{\mathbf{S}} = \tilde{\mathbf{S}}_{\mathrm{a}} + \tilde{\mathbf{S}}_{\mathrm{p}} \tag{2.19}$$

and

$$\overline{\mathbb{C}} = \overline{\mathbb{C}}_{\mathrm{a}} + \overline{\mathbb{C}}_{\mathrm{p}}, \qquad \tilde{\mathbb{C}} = \tilde{\mathbb{C}}_{\mathrm{a}} + \tilde{\mathbb{C}}_{\mathrm{p}}. \tag{2.20}$$

2.2.1. Constitutive Model of the Active Medial Smooth Muscle Cells

We assumed the existence of active smooth muscle fibers consisting of spindle-shaped smooth muscle cells oriented with their longest axis along the muscle fiber direction denoted in the reference configuration by the orientation vector $\mathbf{M}_{\mathrm{cu}}$, as illustrated in Fig. 2.1. The medial layer was modeled as two helically arranged families of smooth muscle fibers embedded in an extra-cellular matrix. The smooth muscle fiber families were oriented symmetrically in the circumferential-axial plane, defined by an angle α_{cu} with respect to the circumferential direction $\mathbf{e}_\theta$, see Fig. 2.1. No dispersion of the smooth muscle fibers in each family was considered.

The contractile apparatus in the smooth muscle cell responsible for the active contraction was modeled by contractile units (CUs), consisting of the actin and myosin filaments, arranged in series oriented to the smooth muscle fiber direction $\mathbf{M}_{\mathrm{cu}}$. The shortening of a CU during activation was caused by ‘cross-bridges’ (CBs) between the actin and myosin

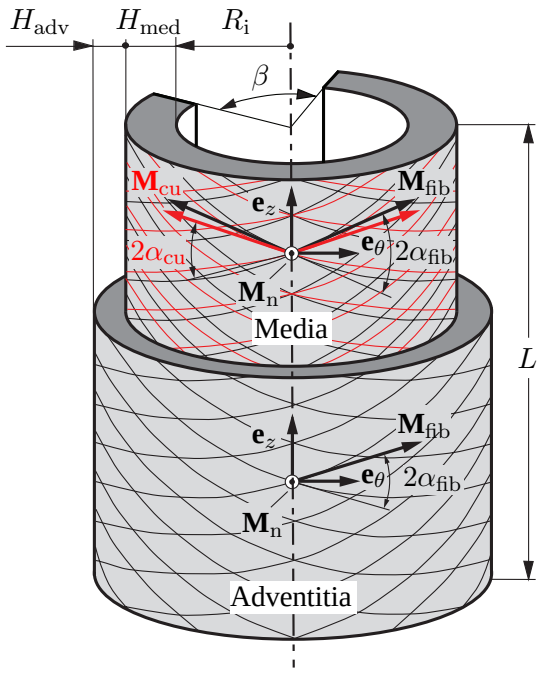

Figure 2.1 Schematic illustration of an abdominal aorta having two layers (modified from Holzapfel et al. (2000)): collagen and smooth muscle fibers form two helically arranged families of fibers each represented by a corresponding direction vector $\mathbf{M}_{\mathrm{fib}}$ and $\mathbf{M}_{\mathrm{cu}}$, making angles α_{fib} and α_{cu} with the circumferential direction $\mathbf{e}_\theta$. Note, that collagen fibers have a large non-rotationally symmetric dispersion around the mean direction vector $\mathbf{M}_{\mathrm{fib}}$, which is laying in the tangential plane (circumferential/axial plane). The normal direction to that plane is denoted by $\mathbf{M}_{\mathrm{n}}$.

filaments causing relative sliding between the filaments. The constitutive model of the smooth muscle cells is based on the work of Murtada and Holzapfel (2014) and Murtada et al. (2010a, 2012) but modified in order to study the effects of the smooth muscle fiber family orientation in the medial layer of the abdominal aorta. In the next sections, a brief summary of the smooth muscle constitutive model is given.

The Chemical Model – Cross-Bridge Kinetics

The activation and kinetics of the CBs was described through the latch-state model proposed by Hai and Murphy (1988). In the latch-state model the CBs were defined through four different functional states, denoted by their corresponding chemical fractions $n_i \geq 0$: (A) dephosphorylated and unattached CBs (n_{M}), (B) phosphorylated and unattached CBs ($n_{\mathrm{M_p}}$), (C) phosphorylated and attached CBs ($n_{\mathrm{AM_p}}$) and (D) dephosphorylated and attached CBs (n_{AM}), which is the so-called latch state, cf. Fig. 2.2. Note that only attached

CBs are able to bear loads. Hai and Murphy (1988) are modeling the CB kinetics through

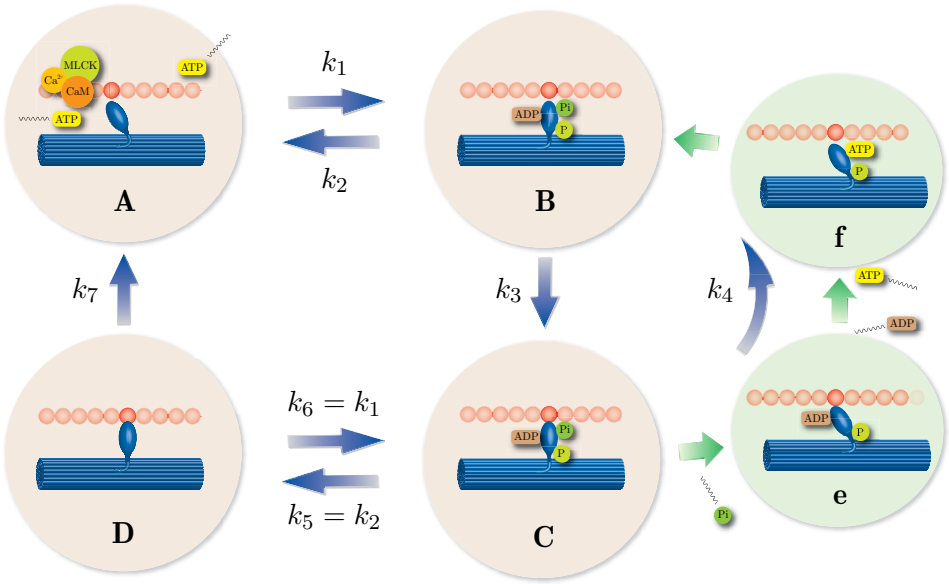

Figure 2.2 Structure of the model by Hai and Murphy (1988). Modified from Murtada et al. (2010a).

a set of ordinary differential equations, which is summarized here in matrix notation

$$\begin{bmatrix} \dot{n}_{\mathrm{M}} \\ \dot{n}_{\mathrm{Mp}} \\ \dot{n}_{\mathrm{AMp}} \\ \dot{n}_{\mathrm{AM}} \end{bmatrix} = \begin{bmatrix} -k_1 & k_2 & 0 & k_7 \\ k_1 & -(k_2+k_3) & k_4 & 0 \\ 0 & k_3 & -(k_4+k_2) & k_1 \\ 0 & 0 & k_2 & -(k_1+k_7) \end{bmatrix} \begin{bmatrix} n_{\mathrm{M}} \\ n_{\mathrm{Mp}} \\ n_{\mathrm{AMp}} \\ n_{\mathrm{AM}} \end{bmatrix}, \tag{2.21}$$

where $k_1, \ldots, k_4$ and k_7 are parameters describing the rate of transition between functional states and the superimposed dots denote time derivatives. The condition $n_{\mathrm{M}}(t) + n_{\mathrm{Mp}}(t) + n_{\mathrm{AMp}}(t) + n_{\mathrm{AM}}(t) = 1$ needs to be satisfied at any time t. According to Hai and Murphy (1988) we assumed that at time $t_0 = 0$ all CBs are in state A, hence $n_{\mathrm{M}}(t_0) = 1$ and $n_{\mathrm{Mp}}(t_0) = n_{\mathrm{AMp}}(t_0) = n_{\mathrm{AM}}(t_0) = 0$. The activating rate parameter k_1 is related to the intracellular calcium concentration $\left[\mathrm{Ca}^{2+}\right]$ and expressed as

$$k_1 = \eta \frac{\left[\mathrm{Ca}^{2+}\right]_i^h}{\left[\mathrm{Ca}^{2+}\right]_i^h + \left[\mathrm{ED}_{50}\right]^h}, \tag{2.22}$$

where ED_{50} is the half-activation constant for calcium, and η and h are fitting parameters. For a more detailed description regarding the CB kinetics model see Hai and Murphy (1988) and Murtada et al. (2010a). The intracellular calcium transient is defined as

$$\left[\mathrm{Ca}^{2+}\right]_i = \begin{cases} 0 & \text{if } t_i < t_1, \\ b + \left[c\,(t_i - t_1) + (a-b)^{-1} - c\,t_2\right]^{-1} & \text{if } t_i > (t_1 + t_2), \\ a\,(t_i - t_1)\,t_2^{-1} & \text{else}, \end{cases} \tag{2.23}$$

where t_1 defines the temporal starting point of the transient, t_2 is the duration until $\left[\mathrm{Ca}^{2+}\right]_i$ reaches the maximum a, and c defines the rate at which $\left[\mathrm{Ca}^{2+}\right]_i$ decreases to the steady state value b.

The Mechanical Model

The mechanical model of the CBs is based on the smooth muscle CU model proposed by Murtada et al. (2012). In that model, the attached load-bearing CBs are modeled as elastic springs with a stiffness constant E_{cb}. Thereby the average elastic elongation $\overline{\mathrm{u}}_{\mathrm{e}}$ of the CBs is defined as

$$\overline{\mathrm{u}}_{\mathrm{e}} = \overline{\lambda}_{\mathrm{cu}} - \overline{\mathrm{u}}_{\mathrm{fs}} - 1, \tag{2.24}$$

where $\overline{\lambda}_{\mathrm{cu}} = l_{\mathrm{cu}}/L_{\mathrm{cu}}$ is the stretch of a CU and $\overline{\mathrm{u}}_{\mathrm{fs}}$ is the relative filament sliding between actin and myosin filaments, see Fig. 2.3.

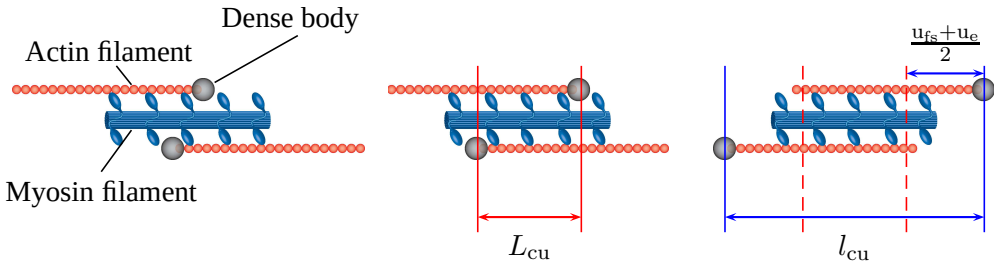

Figure 2.3 Schematic image of a contractile unit (CU). Adopted from Murtada et al. (2012).

The free energy stored in two symmetric families of smooth muscle fibers oriented along the unit vectors $\mathbf{M}_{\mathrm{cu}_i}$ in the reference configuration, as depicted in Fig. 2.1, can be expressed as

$$\overline{\Psi}_{\mathrm{a}}\left(\bar{I}_{\mathrm{cu}_4}, \bar{I}_{\mathrm{cu}_6}\right) = \sum_{i=4,6} \frac{\mu_{\mathrm{a}} \overline{\mathrm{L}}_{\mathrm{fo}_i}}{2} \left(n_{\mathrm{AMp}} + n_{\mathrm{AM}}\right) \left(\sqrt{\bar{I}_{\mathrm{cu}_i}} - \overline{\mathrm{u}}_{\mathrm{fs}_i} - 1\right)^2, \tag{2.25}$$

where the modified pseudo-invariants are

$$\bar{I}_{\mathrm{cu}_i} = \overline{\mathbf{C}} : \mathbf{M}_{\mathrm{cu}_i} \otimes \mathbf{M}_{\mathrm{cu}_i} = \overline{\lambda}^2_{\mathrm{cu}_i} \qquad i = 4, 6. \tag{2.26}$$

The averaged total stiffness of all attached CBs μ_{a} is thereby proportional to the referential length of a single CU L_{cu}, the elastic stiffness of a phosphorylated/dephosphorylated CB E_{cb} and the number of CUs per unit area in the reference configuration N_{cu}. The active force generated within a CU is proportional to the filament overlap $\overline{\mathrm{L}}_{\mathrm{fo}}$ and the relative number of attached load-bearing CBs $(n_{\mathrm{AMp}} + n_{\mathrm{AM}})$.

The relative filament sliding between actin and myosin is described through an evolution law based on Hill's equation for tetanized muscle contraction (Hill, 1938), where the relationship between the shortening velocity and the after-load of an isotonic quick-release test

is described through a hyperbolic function. By assuming that the shortening velocity correlates with the behavior of filament sliding (Guilford and Warshaw, 1998), the evolution law for the relative filament sliding can be expressed by

$$\dot{\overline{\mathrm{u}}}_{\mathrm{fs}_i} = \beta \frac{\mathrm{P}_{\mathrm{a}_i} - \mathrm{P}_{\mathrm{c}_i}}{\mathrm{P}_{\mathrm{a}_i} + \alpha}, \tag{2.27}$$

where α and β are fitting parameters, $\mathrm{P}_{\mathrm{a}_i}$ is the external active first Piola-Kirchhoff stress of one family of smooth muscle fibers in its local direction, i.e.

$$\mathrm{P}_{\mathrm{a}_i} = \frac{\partial \overline{\Psi}_{\mathrm{a}}}{\partial \lambda_{\mathrm{cu}_i}} = \mu_{\mathrm{a}} \overline{\mathrm{L}}_{\mathrm{fo}_i} \left(n_{\mathrm{AMp}} + n_{\mathrm{AM}}\right) \left(\sqrt{\bar{I}_{\mathrm{cu}_i}} - \overline{\mathrm{u}}_{\mathrm{fs}_i} - 1\right), \tag{2.28}$$

and $\mathrm{P}_{\mathrm{c}_i}$ is the internal driving stress from the CBs, which depends on the mechanical state of the contractile unit. The internal driving stress is only dependent on the attached cycling CBs (n_{AMp}) during contraction and dependent on both attached cycling and non-cycling CBs (n_{AMp}, n_{AM}) during relaxation. The internal stress of one family of muscle fibers in its local direction is quantified as

$$\mathrm{P}_{\mathrm{c}_i} = \begin{cases} \overline{\mathrm{L}}_{\mathrm{fo}_i} \kappa_{\mathrm{AMp}} n_{\mathrm{AMp}} & \text{if } \mathrm{P}_{\mathrm{a}_i}^{\mathrm{med}} < \overline{\mathrm{L}}_{\mathrm{fo}_i} \kappa_{\mathrm{AMp}} n_{\mathrm{AMp}}, \\ \overline{\mathrm{L}}_{\mathrm{fo}_i} \left(\kappa_{\mathrm{AMp}} n_{\mathrm{AMp}} + \kappa_{\mathrm{AM}} n_{\mathrm{AM}}\right) & \text{if } \mathrm{P}_{\mathrm{a}_i}^{\mathrm{med}} > \overline{\mathrm{L}}_{\mathrm{fo}_i} \left(\kappa_{\mathrm{AMp}} n_{\mathrm{AMp}} + \kappa_{\mathrm{AM}} n_{\mathrm{AM}}\right), \\ \mathrm{P}_{\mathrm{a}_i} & \text{else}, \end{cases} \tag{2.29}$$

with the stiffness-like material parameters κ_{AMp} and κ_{AM}. Note that according to Murtada et al. (2016b) we set $\kappa_{\mathrm{AM}} = 0.3\kappa_{\mathrm{AMp}}$, implying that cycling CBs determine a stronger contractility than non-cycling CBs. For the relative filament sliding we consider both filament sliding due to any external mechanical loading or deformation, and filament sliding linked to the active cycling CBs. In the case for no attached CBs $\overline{\mathrm{u}}_{\mathrm{fs}} = \overline{\lambda}_{\mathrm{cu}} - 1$.

Filament Overlap

The intracellular structure and organization of the actin and myosin filaments in the smooth muscle CUs are modeled by using a filament overlap function (Murtada et al., 2012). The relative filament overlap $\overline{\mathrm{L}}_{\mathrm{fo}_i}$ between actin and myosin filaments has previously been described using a Gaussian function, which is dependent on the relative filament sliding $\overline{\mathrm{u}}_{\mathrm{fs}_i}$ (Murtada et al., 2016b; Stålhand et al., 2011). We model the filament overlap function using a similar Gaussian function, i.e.

$$\overline{\mathrm{L}}_{\mathrm{fo}_i}\left(\overline{\mathrm{u}}_{\mathrm{fs}_i}\right) = \exp\left[-\frac{\left(\overline{\mathrm{u}}_{\mathrm{fs}_i} - \overline{\mathrm{u}}_{\mathrm{fs}}^{\mathrm{opt}}\right)^2}{2\left(\overline{\mathrm{s}}_{\mathrm{fo}}\right)^2}\right], \tag{2.30}$$

where $\overline{\mathrm{u}}_{\mathrm{fs}}^{\mathrm{opt}}$ is the optimal relative filament sliding value for maximal filament overlap, see Fig. 2.4, and $\overline{\mathrm{s}}_{\mathrm{fo}}$ defines the width of the filament overlap behavior. We model a non-symmetric filament overlap function by adjusting the width parameter $\overline{\mathrm{s}}_{\mathrm{fo}}$ as

$$\overline{\mathrm{s}}_{\mathrm{fo}} = \begin{cases} \overline{\mathrm{s}}_{\mathrm{fo}_1} & \text{if } \overline{\mathrm{u}}_{\mathrm{fs}_i} < \overline{\mathrm{u}}_{\mathrm{fs}}^{\mathrm{opt}}, \\ \overline{\mathrm{s}}_{\mathrm{fo}_2} & \text{else}. \end{cases} \tag{2.31}$$

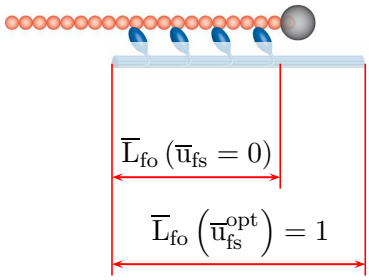

Figure 2.4 Filament overlap behavior $\overline{\mathrm{L}}_{\mathrm{fo}}$: schematic image (modified from Murtada et al. (2012)) shows the initial filament overlap at $\overline{\mathrm{u}}_{\mathrm{fs}}=0$ and the maximum filament overlap at $\overline{\mathrm{u}}_{\mathrm{fs}}=\overline{\mathrm{u}}_{\mathrm{fs}}^{\mathrm{opt}}$.

Active Isochoric Stress and Elasticity Tensor

Since stress and elasticity tensors have already been derived within the continuum mechanical framework section, we focus here on the specific expressions for the active isochoric stress and elasticity tensor, more precisely the fictitious active contributions of the second Piola-Kirchhoff stress tensor and Lagrangian elasticity tensor, see Eqs. (2.19) and (2.20). Therefore, with the use of Eq. (2.26) we obtain

$$\tilde{\mathbf{S}}_{\mathrm{a}}=2\frac{\partial\overline{\Psi}_{\mathrm{a}}}{\partial\overline{\mathbf{C}}}=2\sum_{i=4,\,6}\overline{\Psi}_{\mathrm{a}}'\left(\bar{I}_{\mathrm{cu}_i}\right)\frac{\partial\bar{I}_{\mathrm{cu}_i}}{\partial\overline{\mathbf{C}}}=2\sum_{i=4,\,6}\overline{\Psi}_{\mathrm{a}}'\left(\bar{I}_{\mathrm{cu}_i}\right)\mathbf{M}_{\mathrm{cu}_i}\otimes\mathbf{M}_{\mathrm{cu}_i} \tag{2.32}$$

and

$$\begin{aligned}\tilde{\mathbb{C}}_{\mathrm{a}}&=4\frac{\partial^2\overline{\Psi}_{\mathrm{a}}}{\partial\overline{\mathbf{C}}\,\partial\overline{\mathbf{C}}}=4\sum_{i=4,\,6}\overline{\Psi}_{\mathrm{a}}''\left(\bar{I}_{\mathrm{cu}_i}\right)\frac{\bar{I}_{\mathrm{cu}_i}}{\partial\overline{\mathbf{C}}}\otimes\frac{\bar{I}_{\mathrm{cu}_i}}{\partial\overline{\mathbf{C}}}\\&=4\sum_{i=4,\,6}\overline{\Psi}_{\mathrm{a}}''\left(\bar{I}_{\mathrm{cu}_i}\right)\mathbf{M}_{\mathrm{cu}_i}\otimes\mathbf{M}_{\mathrm{cu}_i}\otimes\mathbf{M}_{\mathrm{cu}_i}\otimes\mathbf{M}_{\mathrm{cu}_i},\end{aligned} \tag{2.33}$$

with the derivatives $\overline{\Psi}_{\mathrm{a}}'\left(\bar{I}_{\mathrm{cu}_i}\right)$ and $\overline{\Psi}_{\mathrm{a}}''\left(\bar{I}_{\mathrm{cu}_i}\right)$ of Eq. (2.25) having the definitions

$$\overline{\Psi}_{\mathrm{a}}'\left(\bar{I}_{\mathrm{cu}_i}\right)=\frac{\partial\overline{\Psi}_{\mathrm{a}}}{\partial\bar{I}_{\mathrm{cu}_i}}=\frac{\mu_{\mathrm{a}}\overline{\mathrm{L}}_{\mathrm{fo}_i}}{2}\left(n_{\mathrm{AMp}}+n_{\mathrm{AM}}\right)\frac{\left(\sqrt{\bar{I}_{\mathrm{cu}_i}}-\overline{\mathrm{u}}_{\mathrm{fs}_i}-1\right)}{\sqrt{\bar{I}_{\mathrm{cu}_i}}} \tag{2.34}$$

and

$$\overline{\Psi}_{\mathrm{a}}''\left(\bar{I}_{\mathrm{cu}_i}\right)=\frac{\partial^2\overline{\Psi}_{\mathrm{a}}}{\partial\bar{I}_{\mathrm{cu}_i}^2}=\frac{\mu_{\mathrm{a}}\overline{\mathrm{L}}_{\mathrm{fo}_i}}{4}\left(n_{\mathrm{AMp}}+n_{\mathrm{AM}}\right)\frac{\overline{\mathrm{u}}_{\mathrm{fs}_i}+1}{\sqrt{\left(\bar{I}_{\mathrm{cu}_i}\right)^3}}. \tag{2.35}$$

2.2.2. Layer Specific Constitutive Model for the Passive Arterial Wall

To capture the layer-specific passive mechanical response of the human abdominal aorta a micro-structural constitutive model recently proposed by Holzapfel et al. (2015) was used, with published mechanical and structural parameters (Niestrawska et al., in press). Briefly, the arterial wall is treated as a thick-walled composite material, i.e. an isotropic groundmatrix containing elastin which is reinforced by two symmetric families of collagen fibers that form a helical structure along the axial direction of the vessel, see Fig. 2.1. Its free-energy function $\overline{\Psi}_{\mathrm{p}}$ can be additively decomposed into an isotropic part $\overline{\Psi}_{\mathrm{g}}$ representing the ground matrix and an anisotropic part $\overline{\Psi}_{\mathrm{fib}}$ characterizing the collagen fibers, i.e.

$$\overline{\Psi}_{\mathrm{p}} = \overline{\Psi}_{\mathrm{g}} + \overline{\Psi}_{\mathrm{fib}}. \tag{2.36}$$

We consider the arterial wall as a two-layered structure, representing the media and the adventitia. The intimal layer is neglected due to its mechanical insignificance compared with the media and the adventitia (Humphrey, 2002). Media and adventitia are characterized by the same form of the free-energy function but with different structural and material parameters. The contribution of the ground substance in Eq. (2.36) is modeled with a neo-Hookean material, i.e.

$$\overline{\Psi}_{\mathrm{g}}\left(\bar{I}_1\right) = \mu_{\mathrm{p}}/2\left(\bar{I}_1 - 3\right), \tag{2.37}$$

where μ_{p} is the shear modulus and $\bar{I}_1$ the modified principal strain invariant introduced in Eq. (2.2). A second-order structure tensor for each collagen fiber family $\mathbf{H}_i$, $i = 4, 6$, is introduced in the material description, which is defined in terms of the mean (in-plane) direction vector $\mathbf{M}_{\mathrm{fib}_i}$ lying in the tangential plane, the out-of-plane direction vector $\mathbf{M}_{\mathrm{n}}$ and the second-order identity tensor $\mathbf{I}$. Thus,

$$\mathbf{H}_i = A\mathbf{I} + B\mathbf{M}_{\mathrm{fib}_i} \otimes \mathbf{M}_{\mathrm{fib}_i} + (1 - 3A - B)\,\mathbf{M}_{\mathrm{n}} \otimes \mathbf{M}_{\mathrm{n}}, \tag{2.38}$$

where $A = 2\kappa_{\mathrm{op}}\kappa_{\mathrm{ip}}$ and $B = 2\kappa_{\mathrm{op}}\left(1 - 2\kappa_{\mathrm{ip}}\right)$ contain the in-plane dispersion parameter κ_{ip} and the out-of-plane dispersion parameter κ_{op}. The anisotropic part of the free-energy function as given in Eq. (2.36) is reflecting the mechanical behavior of collagen fibers. Thus,

$$\overline{\Psi}_{\mathrm{fib}}\left(\bar{I}^{\star}_{\mathrm{fib}_i}\right) = \frac{C_1}{2C_2}\sum_{i=4,6}\left\{\exp\left[C_2\big(\bar{I}^{\star}_{\mathrm{fib}_i} - 1\big)^2\right] - 1\right\}, \qquad i = 4, 6, \tag{2.39}$$

where C_1 is a positive stress-like material parameter and C_2 is a positive dimensionless material parameter. Further, the unimodular generalized invariants are defined as

$$\bar{I}^{\star}_{\mathrm{fib}_i} = \overline{\mathbf{C}} : \mathbf{H}_i = A\bar{I}_1 + B\bar{I}_{\mathrm{fib}_i} + (1 - 3A - B)\,\bar{I}_{\mathrm{n}}, \tag{2.40}$$

together with the unimodular pseudo-invariants $\bar{I}_{\mathrm{fib}_i} = \overline{\mathbf{C}} : \mathbf{M}_{\mathrm{fib}_i} \otimes \mathbf{M}_{\mathrm{fib}_i} = \overline{\lambda}^2_{\mathrm{fib}_i}$ and $\bar{I}_{\mathrm{n}} = \overline{\mathbf{C}} : \mathbf{M}_{\mathrm{n}} \otimes \mathbf{M}_{\mathrm{n}} = \overline{\lambda}^2_{\mathrm{n}}$, $i = 4, 6$, representing the squares of the unimodular stretches in the mean fiber direction and the out-of-plane direction, respectively.

Note that according to Holzapfel et al. (2000) it is assumed that the anisotropic term, as shown in Eq. (2.39), only contributes to $\overline{\Psi}_{\mathrm{p}}$ if the corresponding fibers are under tension.

The fictitious passive contributions of the second Piola-Kirchhoff stress tensor $\tilde{\mathbf{S}}_{\mathrm{p}}$ and the Lagrangian elasticity tensor $\tilde{\mathbb{C}}_{\mathrm{p}}$, as shown in Eqs. (2.19) and (2.20), can be expressed with the use of Eqs. (2.2), (2.38) and (2.40) as

$$\begin{aligned}\tilde{\mathbf{S}}_{\mathrm{p}} &= 2\frac{\partial\overline{\Psi}_{\mathrm{p}}}{\partial\overline{\mathbf{C}}} = 2\left(\frac{\partial\overline{\Psi}_{\mathrm{g}}}{\partial\bar{I}_1}\frac{\partial\bar{I}_1}{\partial\overline{\mathbf{C}}} + \sum_{i=4,\,6}\overline{\Psi}'_{\mathrm{fib}}\left(\bar{I}^{\star}_{\mathrm{fib}_i}\right)\frac{\partial\bar{I}^{\star}_{\mathrm{fib}_i}}{\partial\overline{\mathbf{C}}}\right)\\ &= 2\left(\frac{\mu_{\mathrm{p}}}{2}\mathbf{I} + \sum_{i=4,\,6}\overline{\Psi}'_{\mathrm{fib}}\left(\bar{I}^{\star}_{\mathrm{fib}_i}\right)\mathbf{H}_i\right)\end{aligned} \tag{2.41}$$

and

$$\begin{aligned}\tilde{\mathbb{C}}_{\mathrm{p}} &= 4\frac{\partial^2\overline{\Psi}_{\mathrm{p}}}{\partial\overline{\mathbf{C}}\,\partial\overline{\mathbf{C}}} = 4\sum_{i=4,\,6}\overline{\Psi}''_{\mathrm{fib}}\left(\bar{I}^{\star}_{\mathrm{fib}_i}\right)\frac{\partial\bar{I}^{\star}_{\mathrm{fib}_i}}{\partial\overline{\mathbf{C}}}\otimes\frac{\partial\bar{I}^{\star}_{\mathrm{fib}_i}}{\partial\overline{\mathbf{C}}}\\ &= 4\sum_{i=4,\,6}\overline{\Psi}''_{\mathrm{fib}}\left(\bar{I}^{\star}_{\mathrm{fib}_i}\right)\mathbf{H}_i\otimes\mathbf{H}_i,\end{aligned} \tag{2.42}$$

with the derivatives $\overline{\Psi}'_{\mathrm{fib}}\left(\bar{I}^{\star}_{\mathrm{fib}_i}\right)$ and $\overline{\Psi}''_{\mathrm{fib}}\left(\bar{I}^{\star}_{\mathrm{fib}_i}\right)$ of Eq. (2.39) with respect to $\bar{I}^{\star}_{\mathrm{fib}_i}$ defined as

$$\overline{\Psi}'_{\mathrm{fib}}\left(\bar{I}^{\star}_{\mathrm{fib}_i}\right) = \frac{\partial\overline{\Psi}_{\mathrm{fib}}}{\partial\bar{I}^{\star}_{\mathrm{fib}_i}} = C_1\left(\bar{I}^{\star}_{\mathrm{fib}_i}-1\right)\exp\left[C_2\left(\bar{I}^{\star}_{\mathrm{fib}_i}-1\right)^2\right] \tag{2.43}$$

and

$$\overline{\Psi}''_{\mathrm{fib}}\left(\bar{I}^{\star}_{\mathrm{fib}_i}\right) = \frac{\partial^2\overline{\Psi}_{\mathrm{fib}}}{\partial\bar{I}^{\star 2}_{\mathrm{fib}_i}} = C_1\left[1+2C_2\left(\bar{I}^{\star}_{\mathrm{fib}_i}-1\right)^2\right]\exp\left[C_2\left(\bar{I}^{\star}_{\mathrm{fib}_i}-1\right)^2\right]. \tag{2.44}$$

2.3. Parameter Identification

The stiffness parameter κ_{AMp} is expressed in terms of μ_{a} through the relationship between the external mechanical force and the internal driving force from the evolution law at steady state, i.e. $\dot{\overline{\mathrm{u}}}_{\mathrm{fs}} = 0$. Therefore,

$$\kappa_{\mathrm{AMp}}\left(\mu_{\mathrm{a}}\right) = \mu_{\mathrm{a}}\left(\frac{n_{\mathrm{AMp,ss}}+n_{\mathrm{AM,ss}}}{n_{\mathrm{AMp,ss}}}\right)\overline{\mathrm{u}}_{\mathrm{e,ss}}, \tag{2.45}$$

where $n_{\mathrm{AMp,ss}}$ and $n_{\mathrm{AM,ss}}$ are the corresponding chemical fractions at steady state. The active material parameters μ_{a}, $\overline{\mathrm{u}}^{\mathrm{opt}}_{\mathrm{fs}}$, $\overline{\mathrm{s}}_{\mathrm{fo}_1}$ and $\overline{\mathrm{s}}_{\mathrm{fo}_2}$ for a given smooth muscle fiber orientation are obtained from the modified experimental tension-time and length-tension behavior using a nonlinear least-squares minimization of the error e, defined as

$$e\left(\mu_{\mathrm{a}},\overline{\mathrm{u}}^{\mathrm{opt}}_{\mathrm{fs}},\overline{\mathrm{s}}_{\mathrm{fo}_1},\overline{\mathrm{s}}_{\mathrm{fo}_2}\right) = \sum_{i=1}^{m}\left(\frac{P^{\mathrm{mod}}_{\theta\theta,i}-P^{\mathrm{exp}}_{\theta\theta,i}}{\hat{P}^{\mathrm{exp}}_{\theta\theta}}\right)^2 + \sum_{j=1}^{n}\left(\frac{P^{\mathrm{mod,ss}}_{\theta\theta,j}-P^{\mathrm{exp,ss}}_{\theta\theta,j}}{\hat{P}^{\mathrm{exp,ss}}_{\theta\theta}}\right)^2, \tag{2.46}$$

where $P^{\mathrm{mod}}_{\theta\theta,i}$, $P^{\mathrm{exp}}_{\theta\theta,i}$ denote the first Piola-Kirchhoff stress in the circumferential direction as a function of time for the model and experimental value, respectively, (m is the number of data points), $P^{\mathrm{mod,ss}}_{\theta\theta,j}$, $P^{\mathrm{exp,ss}}_{\theta\theta,j}$ are the first Piola-Kirchhoff stress in the circumferential direction at steady state for different stretches for the model and experimental value (n is the number of length-tension data points, i.e. experiments using different pre-stretches $\lambda_\theta = [1.0, 1.56]$). The hat on the experimental stress values stands for the mean values over all data points i and j. Explicit analytical expressions are used for the fitting and summarized in the Appendix B. A regression analysis is performed in MATLAB using the built-in function *lsqnonlin* and assigning random initial guesses and appropriate physical constraints on the parameters. A minimum of six minimization cycles ensured that best-fit parameters are independent of initial guesses (Ferruzzi et al., 2015). The accuracy of the experimental data fit of the proposed model is illustrated by determining a squared residual parameter (coefficient of determination), denoted by

$$R^2 = 1 - \frac{\mathrm{SS}_{\mathrm{res}}}{\mathrm{SS}_{\mathrm{tot}}} = 1 - \frac{\sum_{k=1}^{(m+n)} \left(f_k^{\mathrm{mod}} - f_k^{\mathrm{exp}}\right)^2}{\sum_{k=1}^{(m+n)} \left(f_k^{\mathrm{exp}} - \frac{1}{(m+n)} \sum_{k=1}^{n} f_k^{\mathrm{exp}}\right)^2}, \tag{2.47}$$

with $0 \leq R^2 \leq 1$, where a value of one indicates a perfect fit to the experimental data and the more it tends towards zero the poorer the fit gets. Note that f_k includes the data points $P_{\theta\theta}$ and $P^{\mathrm{ss}}_{\theta\theta}$, as used in Eq. (2.46).

2.4. Implementation into a Finite Element Program

The proposed constitutive models to describe the passive and active arterial wall behavior are implemented into the multipurpose finite element program FEAP (Taylor, 2013). For each time step ($\Delta t = \textit{const.}$) and at each integration point the update algorithm, as shown in Table 2.1, is performed.

Table 2.1 *Update algorithm performed for each time step and integration point*

1. Read history variables: n_{M}, n_{Mp}, n_{AMp}, n_{AM}, $\overline{\mathrm{u}}_{\mathrm{e}_4}$, $\overline{\mathrm{u}}_{\mathrm{e}_6}$, $\overline{\mathrm{u}}_{\mathrm{fs}_4}$, $\overline{\mathrm{u}}_{\mathrm{fs}_6}$
2. Update the calcium concentration $\left[\mathrm{Ca}^{2+}\right]$ from Eq. (2.23) and calculate the current rate constant k_1 using Eq. (2.22)
3. Compute new fractions of attached cross-bridges (n_{AMp}, n_{AM}) by solving the system of ODEs given in Eq. (2.21), using an Euler scheme.
4. Calculate the current unimodular pseudo-invariants $\bar{I}_{\mathrm{cu}_4}$ and $\bar{I}_{\mathrm{cu}_6}$ from Eq. (2.26)
5. Mechanical update of the relative filament slidings $\overline{\mathrm{u}}_{\mathrm{fs}_4}$ and $\overline{\mathrm{u}}_{\mathrm{fs}_6}$ according to step (3) by means of Eq. (2.24) using the average elastic elongations from the previous time step (history variables $\overline{\mathrm{u}}_{\mathrm{e}_4}$ and $\overline{\mathrm{u}}_{\mathrm{e}_6}$)
6. Calculate the filament overlaps $\overline{\mathrm{L}}_{\mathrm{fo}_4}$ and $\overline{\mathrm{L}}_{\mathrm{fo}_6}$, the active external stresses $\mathrm{P}_{\mathrm{a}_4}$ and $\mathrm{P}_{\mathrm{a}_6}$, the internal driving stresses $\mathrm{P}_{\mathrm{c}_4}$ and $\mathrm{P}_{\mathrm{c}_6}$, using Eqs. (2.30), (2.31), (2.28) and (2.29)
7. Chemical update of the relative filament slidings $\overline{\mathrm{u}}_{\mathrm{fs}_4}$ and $\overline{\mathrm{u}}_{\mathrm{fs}_6}$ by solving the evolution law (2.27) using an Euler scheme
8. Update the average elastic elongations $\overline{\mathrm{u}}_{\mathrm{e}_4}$ and $\overline{\mathrm{u}}_{\mathrm{e}_6}$, the filament overlaps $\overline{\mathrm{L}}_{\mathrm{fo}_4}$ and $\overline{\mathrm{L}}_{\mathrm{fo}_6}$, using Eqs. (2.24), (2.30) and (2.31)
9. Compute the stress tensor **S** and the elasticity tensor $\mathbb{C}$, using Eqs. (2.6) and (2.11)
8. Store updated history variables: n_{M}, n_{Mp}, n_{AMp}, n_{AM}, $\overline{\mathrm{u}}_{\mathrm{e}_4}$, $\overline{\mathrm{u}}_{\mathrm{e}_6}$, $\overline{\mathrm{u}}_{\mathrm{fs}_4}$, $\overline{\mathrm{u}}_{\mathrm{fs}_6}$

2.5. Representative Finite Element Simulations

Two representative examples are simulated and analyzed using the finite element implementation of the proposed smooth muscle fiber model, and are subsequently described.

2.5.1. Uniaxial Isometric Contraction of an Aortic Medial Strip

The isometric contraction of smooth muscles in a medial strip of the human abdominal aorta, activated through a calcium transient is simulated in the first example. The main purpose of this numerical example is a validation of the model implementation. There-

fore, finite element results are compared with the one-dimensional simulation solved with MATLAB. Due to symmetry, only one half of the medial strip is modeled. We use 1000 eight-node hexahedral elements, applying the mixed Q1/P0 element formulation throughout the computation, to avoid locking phenomena. All nodes are constrained in all directions at one end of the strip and constrained only in the circumferential direction at the other end of the modeled strip. A linearly increasing circumferential stretch is initially applied to the modeled strip, and subsequently contracted through a realistic calcium concentration transient. The calcium transient is identical to that used for fitting, see Eq. (2.23).

2.5.2. Inflation and Contraction of an Arterial Ring

In the second example the pressure-radius relationship and the transmural stress distributions of a residually stressed arterial ring with two layers (media and adventitia), subjected to axial pre-stretch, internal pressure and smooth muscle contraction are studied. The impact of the smooth muscle fiber orientation α_{cu} on the mechanical behavior of the human abdominal aorta is investigated for different sets of smooth muscle material parameters. In particular the effects of the smooth muscle stiffness μ_{a} and the filament overlap function ($\overline{\mathrm{u}}_{\mathrm{fs}}^{\mathrm{opt}}$, $\overline{\mathrm{s}}_{\mathrm{fo}_1}$, $\overline{\mathrm{s}}_{\mathrm{fo}_2}$) on the pressure-radius relationship and the transmural wall stresses are analyzed. In order to consider residual stresses (and strains), the stress-free reference configuration of the arterial ring is modeled with an opening angle β, see Fig. 2.1. The symmetrical boundary conditions constrained the cross-sectional surfaces of the arterial ring in the circumferential direction. The axial stretch is kept constant during inflation and contraction.

3. Results

3.1. Parameter Identification

Parameters for the chemical model (see Eqs. (2.21) and (2.22)) are taken from Murtada and Holzapfel (2014) and summarized in Table 3.1. In order to estimate the material parameters for the proposed active constitutive model, experimental active length-tension data of the pig common carotid arteries presented in Murtada et al. (2012) are adopted. Due to the fact that there are no suitable experimental data available on the contractile behavior of human aortic tissue so far the active length-tension and tension-time data are chosen and modified slightly, see Appendix C.

Table 3.1 *Parameters for the chemical model, taken from Murtada and Holzapfel (2014)*

Kinetics model						
$\eta\,[\mathrm{s}^{-1}]$	$h\,$[-]	$\mathrm{ED}_{50}\,[\mu\mathrm{Mol}]$	$k_2\,[\mathrm{s}^{-1}]$	$k_3\,[\mathrm{s}^{-1}]$	$k_4\,[\mathrm{s}^{-1}]$	$k_7\,[\mathrm{s}^{-1}]$
0.35917	4	0.37	0.16267	0.06667	0.00083	0.00667
Calcium transient						
$t_1\,$[s]	$t_2\,$[s]	$a\,$[nMol]	$b\,$[nMol]	$c\,[(\mu\mathrm{Mol\ s})^{-1}]$		
60	6	400	300	1		

The average elastic elongation at steady state is set to $\overline{\mathrm{u}}_{\mathrm{e,ss}} = 0.02$, according to Arner (1982), and the parameters α and β used in Eq. (2.27) are set to values which are taken from Murtada et al. (2012), i.e. $\alpha = 26.68\,\mathrm{kPa}$ and $\beta = 0.00833\,\mathrm{s}^{-1}$. Material and structural parameters for the proposed passive constitutive model were taken from Niestrawska et al. (in press), and are summarized in Table 3.2. Micro-structural investigations (second-harmonic generation imaging) as well as biaxial mechanical tensile tests of healthy abdominal aortas are performed, and the experimental data are fitted to the same non-symmetric collagen fiber dispersion model used in this work.

Table 3.2 *Passive material and structural parameters for the media and adventitia of the healthy abdominal aorta (median), taken from Niestrawska et al. (in press)*

Layer	Material parameters			Structural parameters		
	μ_{p} [kPa]	C_1 [kPa]	C_2 [-]	κ_{ip} [-]	κ_{op} [-]	α_{fib} [°]
Media	16.08	11.68	7.18	0.208	0.487	6.91
Adventitia	3.77	0.36	45.88	0.232	0.466	77.53

3.2. The Impact of Smooth Muscle Fiber Orientation and Filament Overlap Behavior on the Fitting of Active Material Parameters

The relationship between the filament overlap function and the smooth muscle cell orientation was investigated by studying the squared residual parameter R^2 of the stretch-active stress behavior for different smooth muscle cell orientation angles α_{cu}. The non-symmetric filament overlap function resulted in a better fit for smaller values of the smooth muscle fiber orientation. However, no difference in the simulated length-tension behavior using the symmetric and non-symmetric filament overlap function was observed for $\alpha_{\mathrm{cu}} \geq 30°$, see Fig. 3.1(a). Figure 3.1(b) shows that for a smooth muscle fiber orientation of $\alpha_{\mathrm{cu}} = 0°$ a non-symmetric filament overlap function (solid curve) was able to simulate a better fit to the experimental active length-tension behavior (circles) than a symmetric filament overlap function (dashed curve), especially at higher stretches.

The fitted active material parameters for different smooth muscle fiber orientations are presented in Fig. 3.2. An increase in the stiffness parameter μ_{a} was estimated with increasing muscle fiber orientation α_{cu} in order to maintain the same circumferential isometric contractile tension as observed for the circumferentially aligned smooth muscle fibers. Figure 3.2(b) illustrates the behavior of the material parameters used in the filament overlap function, Eq. (2.30). All three parameters $\overline{\mathrm{u}}_{\mathrm{fs}}^{\mathrm{opt}}$, $\overline{\mathrm{s}}_{\mathrm{fo}_1}$ and $\overline{\mathrm{s}}_{\mathrm{fo}_2}$ decreased with an increasing smooth muscle fiber orientation α_{cu}. The filament overlap function parameters decreased with increasing α_{cu} where the width parameters reached equivalent values for smooth muscle fiber angles larger than $30°$. Interestingly, the optimal filament parameter $\overline{\mathrm{u}}_{\mathrm{fs}}^{\mathrm{opt}}$ decreased for increasing values of smooth muscle fiber orientation α_{cu} suggesting that the optimal stretch for maximal filament overlap was reached closer to resting muscle length for smooth muscle fiber orientation values near $\alpha_{\mathrm{cu}} = 40°$. In Tab. 3.3 material parameters for the proposed active constitutive model are summarized for several different smooth muscle fiber orientations α_{cu}.

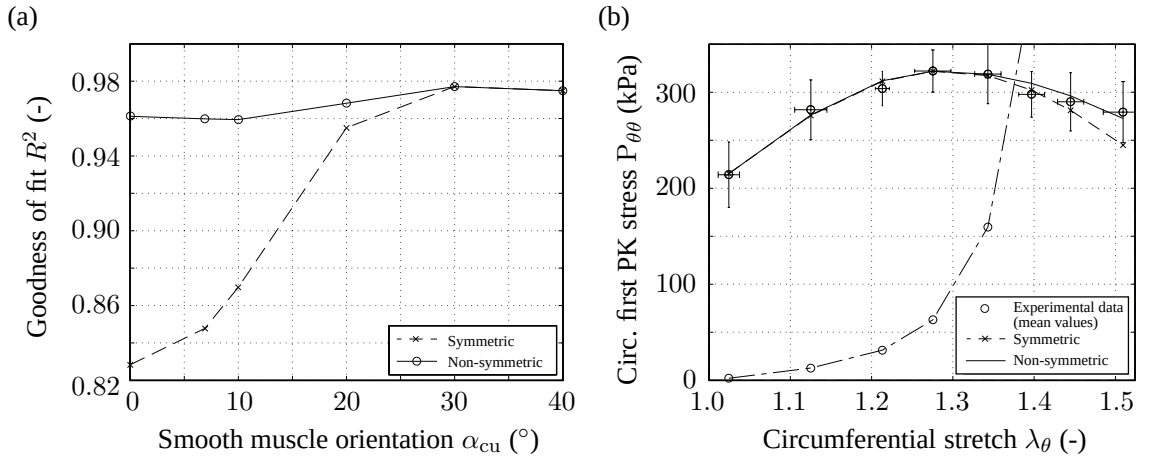

Figure 3.1 Fitting results: (a) R^2 values as a function of smooth muscle orientation for both symmetric and non-symmetric filament overlap functions; (b) active (dashed and solid curves) and passive (dash-dotted curve) length-tension behavior for circumferentially oriented smooth muscle fibers ($\alpha_{\mathrm{cu}} = 0°$). The dashed curve represents the active model behavior using a symmetric filament overlap function, while the solid curve shows results for the model using a non-symmetric function. Circles indicate experimental mean values, with corresponding standard deviations.

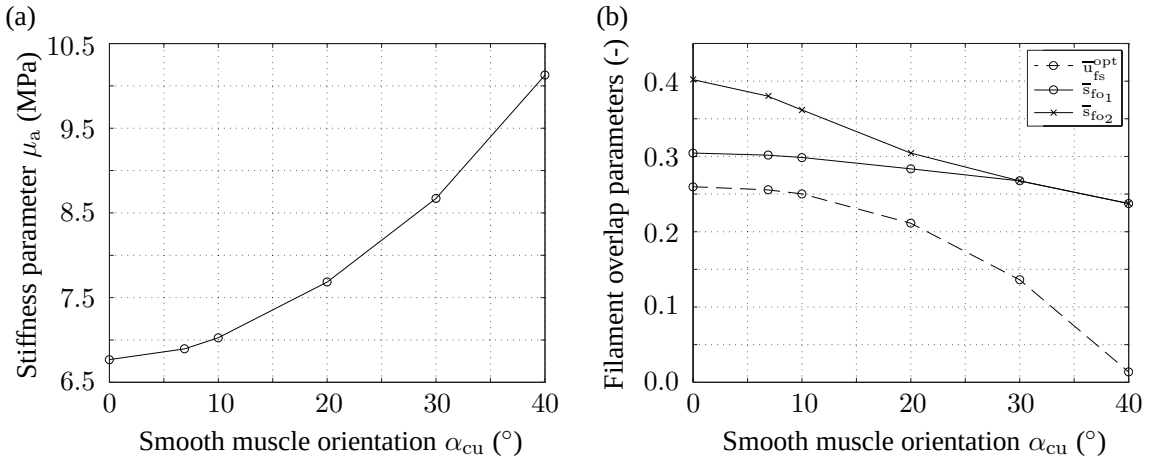

Figure 3.2 Influence of different smooth muscle fiber orientations α_{cu} on the stiffness parameter μ_{a}, and the filament overlap parameters $\overline{\mathrm{u}}_{\mathrm{fs}}^{\mathrm{opt}}$, $\overline{\mathrm{s}}_{\mathrm{fo}_1}$ and $\overline{\mathrm{s}}_{\mathrm{fo}_2}$.

Table 3.3 *Set of active material parameters for different smooth muscle orientations*

α_{cu}	Fitted parameters				Related and fixed parameters		
	μ_{a} [MPa]	$\overline{\mathrm{u}}_{\mathrm{fs}}^{\mathrm{opt}}$ [-]	$\overline{\mathrm{s}}_{\mathrm{fo}_1}$ [-]	$\overline{\mathrm{s}}_{\mathrm{fo}_2}$ [-]	κ_{AMp} [kPa]	α [kPa]	β [s^{-1}]
0°	6.768	0.260	0.305	0.402	319.995	26.68	0.00833
6.91°	6.895	0.256	0.302	0.380	326.010		
10°	7.026	0.250	0.299	0.362	332.221		
20°	7.683	0.211	0.284	0.305	363.262		
30°	8.671	0.136	0.268	0.268	409.976		
40°	10.126	0.014	0.238	0.238	478.776		

3.3. Uniaxial Isometric Contraction of an Aortic Medial Strip – Validation of Model Implementation

A medial strip is modeled with a referential length $L = 15.0\,\mathrm{mm}$ (circ. direction), referential width $W = 3.0\,\mathrm{mm}$ (axial direction) and referential thickness $H_{\mathrm{med}} = 0.8467\,\mathrm{mm}$ (Niestrawska et al., in press). All finite element results are taken from a central node located at the end of the modeled strip, where only one degree of freedom is constrained, and then they are compared with the one-dimensional solution calculated in MATLAB. The implementation of the cross-bridge kinetics model is verified by comparing the finite element analysis with the one-dimensional simulation triggered by one specific calcium concentration, see Fig. 3.3(a). The circumferential Cauchy stress is also compared and verified between the two simulations of a strip with smooth muscle fiber orientation $\alpha_{\mathrm{cu}} = 30^\circ$, see Fig. 3.3(b). The relative error between the finite element simulation and the one-dimensional solution for all smooth muscle fiber orientations was less than 1 percent.

The distribution of the circumferential Cauchy stress obtained from the finite element analysis for half the volume of a medial strip is presented with relaxed smooth muscle fibers (Fig. 3.4(a)), and with contracted smooth muscle fibers having fiber orientations $\alpha_{\mathrm{cu}} = 0^\circ$ (Fig. 3.4(b)) and $\alpha_{\mathrm{cu}} = 30^\circ$ (Fig. 3.4(c)). Note that for both simulations ($\alpha_{\mathrm{cu}} = 0^\circ$ and $\alpha_{\mathrm{cu}} = 30^\circ$) different active material parameters are used, see Table 3.3. The medial strip simulation with a smooth muscle fiber orientation of $\alpha_{\mathrm{cu}} = 30^\circ$ resulted in a larger change in width and increased thickness at the contracted state compared with the simulation with smooth muscle fiber orientation $\alpha_{\mathrm{cu}} = 0^\circ$.

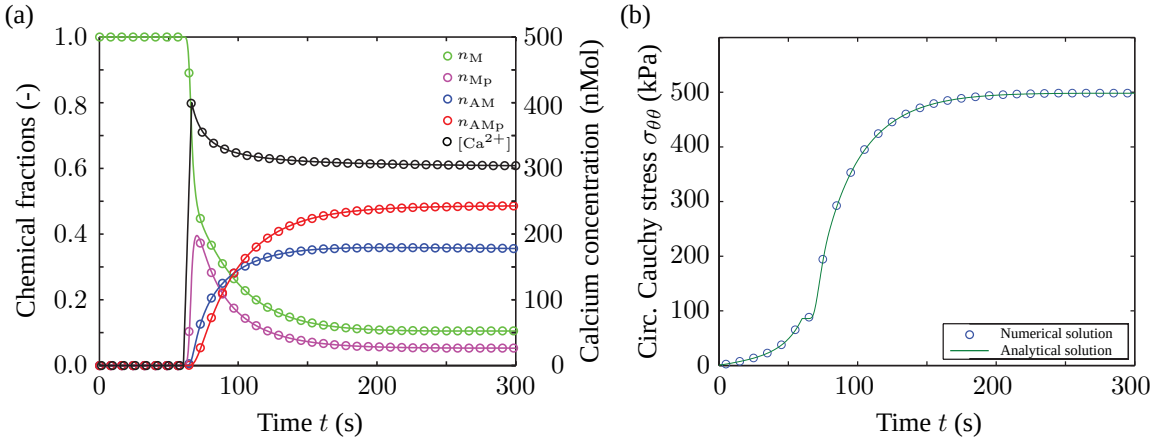

Figure 3.3 Verification of the material model implementation – changes of chemical and mechanical quantities in a medial strip during contraction over a time period of 300 seconds: (a) time dependent intra-cellular calcium concentration and chemical fractions of myosin heads for the states A, B, C and D; (b) Cauchy stress in the circumferential direction; circles represent finite element results, while the solid curve is an analytical result for the one-dimensional solution.

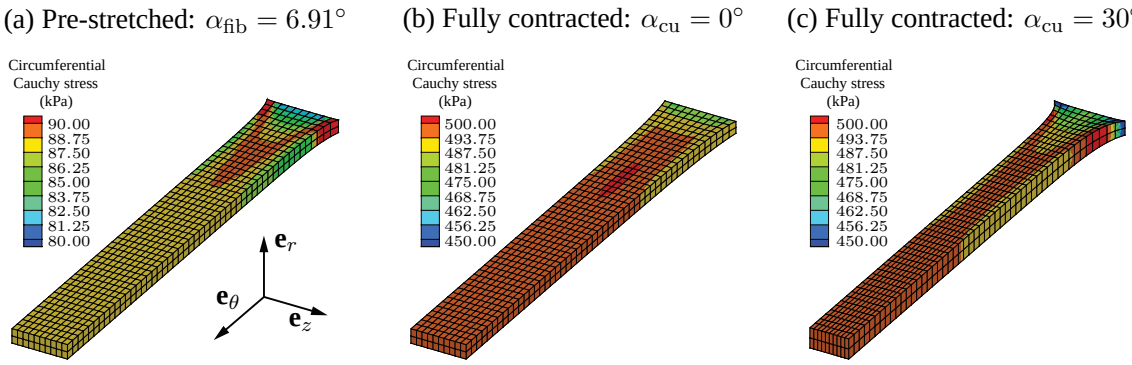

Figure 3.4 Three-dimensional Cauchy stress distribution in the circumferential direction of the medial strip with two symmetric families of collagen and smooth muscle fibers. Results are shown at the end of the passive pre-stretch phase: (a) at $t = 60$ seconds; (b),(c) at the end of the active smooth muscle contraction phase at $t = 300$ seconds for $\alpha_{\mathrm{cu}} = 0°$ and $\alpha_{\mathrm{cu}} = 30°$.

3.4. Inflation and Contraction of an Arterial Ring

For this numerical investigation the abdominal aorta was modeled as a half ring under plane strain conditions with an opening angle $\beta = 60°$. The inner radius of the ring was set to $R_{\mathrm{i}} = 6.8375\,\mathrm{mm}$ (Holzapfel and Ogden, 2010; Holzapfel et al., 2007), the medial wall thicknesses is $H_{\mathrm{med}} = 0.8467\,\mathrm{mm}$ and the adventitial wall thickness is $H_{\mathrm{adv}} = 0.5884\,\mathrm{mm}$ (Niestrawska et al., in press) in the reference configuration. Due to symmetry only one half of the whole arterial ring was simulated and discretized by 640 eight-node hexahedral elements (320 elements per layer), applying the mixed $Q1/P0$ element formulation throughout the simulation. All nodes at the media/adventitia interface were linked together. The collagen and smooth muscle fiber orientations were defined in the unloaded and stress-free reference configuration, and the values are provided in Tables 3.2 and 3.4.

Table 3.4 *Set of active material parameters used for the simulations*

Set	α_{cu}	μ_{a} [MPa]	κ_{AMp} [kPa]	$\overline{\mathrm{u}}_{\mathrm{fs}}^{\mathrm{opt}}$ [-]	$\overline{\mathrm{s}}_{\mathrm{fo}_1}$ [-]	$\overline{\mathrm{s}}_{\mathrm{fo}_2}$ [-]
1	$0°$	6.8	320	0.26	0.30	0.40
2				0.14	0.27	0.27
$2a$				0.14	0.27	0.80
$2b$				0.14	0.80	0.27
$2c$				0.07	0.27	0.27
3		8.7	410	0.26	0.30	0.40
4	$30°$	6.8	320	0.26	0.30	0.40
5				0.14	0.27	0.27
6		8.7	410	0.26	0.30	0.40

The meshed arterial ring in the load- and stress free reference configuration is presented in Fig. 3.5(a). The opening angle of the arterial ring was initially closed and then the ring was pre-stretched with 1.0675 in the axial direction (Horný et al., 2014) (Fig. 3.5(b)), pressurized to a certain level (Fig. 3.5(c)), and contracted (Fig. 3.5(d)). The contraction was triggered with a constant calcium concentration of $170\,\mathrm{nMol}$. This procedure was repeated for different pressure values. The circumferential stress distribution of the arterial wall at different simulation states is presented in Fig. 3.5.

The internal pressure-inner radius relationship of an arterial ring at the relaxed and the contracted states was analyzed for different structural and mechanical smooth muscle properties as defined in Tab. 3.4, see Fig. 3.6(a). Eight different cases were studied: two passive pressure-radius relationships with and without residual stresses and six active pressure-radius relationships with different smooth muscle fiber orientations and sets of material parameters. A change in the smooth muscle fiber orientation without changing the material parameters resulted in a reduced contraction in the circumferential direction, and hence a larger inner radius compared to simulations with circumferentially aligned smooth muscle

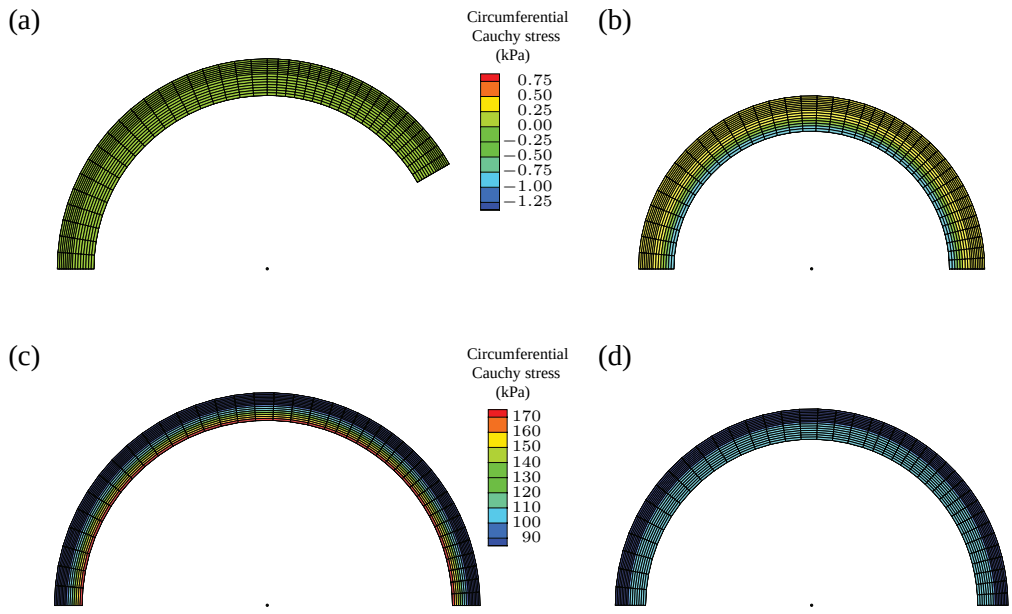

Figure 3.5 Contour plots representing the circumferential Cauchy stress distribution of the human abdominal aortic ring at different simulation states: (a) the load- and stress-free reference configuration; (b) the residually stressed and axially pre-stretched state; (c) at an internal blood pressure of $90\,\text{mmHg}$; (d) when smooth muscle cells are fully contracted. Note that in (a) and (b) as well as in (c) and (d) the same stress legend is used.

fibers. A decrease in the filament overlap parameter $\overline{\mathrm{u}}_{\mathrm{fs}}^{\mathrm{opt}}$ resulted in a stronger contraction at the low pressure domain ($\leq 90\,\text{mmHg}$), and the filament overlap width parameters $\overline{\mathrm{s}}_{\mathrm{fo}_1}$ and $\overline{\mathrm{s}}_{\mathrm{fo}_2}$ had a significant effect on the shape of the pressure-radius relationship.

Figure 3.6(b) shows corresponding transmural circumferential and axial Cauchy stress distributions of the medial layer at an internal pressure of $90\,\text{mmHg}$. The negative transmural circumferential stress gradient, with larger stress values closer to the lumen was reduced after inclusion of residual stresses in the ring, and it completely vanished by including the active tone contributed by the smooth muscle cells. With increasing active tone, the transmural stress gradient could even turn positive, with smaller stress values closer to the lumen. The residually stressed and axially pre-stretched inflated arterial ring had a slightly negative axial stress gradient with a positive averaged axial stress value, i.e. axial tensile stress. This stress gradient is again smaller than the gradient of the arterial ring that does not consider residual stresses. After smooth muscle contraction it becomes marginally positive. The arterial ring simulations with a muscle fiber orientation of $\alpha_{\mathrm{cu}} = 30^{\circ}$ showed an averaged axial stress similar to that of the relaxed state in contrast to the arterial rings having circumferentially aligned muscle fibers.

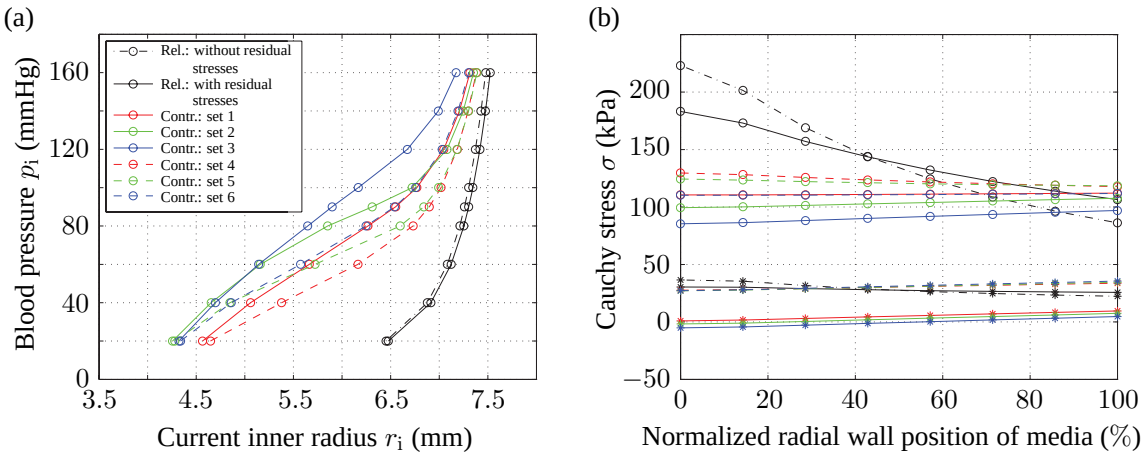

Figure 3.6 Influence of changes in smooth muscle orientation and active material parameters on the mechanical behavior: (a) blood pressure as a function of the current inner radius for the relaxed and contracted state; (b) distribution of the circumferential (circles) and axial (asterisks) Cauchy stress over the normalized medial wall thickness at an internal blood pressure of 90 mmHg. Curves of the same color are based on the same material parameters, but different smooth muscle orientations, i.e. $\alpha_{\mathrm{cu}} = 0°$ (solid), $\alpha_{\mathrm{cu}} = 30°$ (dashed). The solid black curve represents the passive mechanical response considering residual stresses, while the dash-dotted black curve does not consider them.

Figures 3.7 and 3.8 highlight the influence of alterations of the filament overlap parameters on the filament overlap behavior and the pressure-radius relationship. A significantly increased non-symmetry of the filament overlap function caused by an increase of $\overline{\mathrm{s}}_{\mathrm{fo}_2}$ shows a slightly stronger contractile behavior at the pressure domain above 90 mmHg, while the increased $\overline{\mathrm{s}}_{\mathrm{fo}_1}$ resulted in a very strong muscle contraction at the pressure domain below 90 mmHg. When $\overline{\mathrm{u}}_{\mathrm{fs}}^{\mathrm{opt}}$ was reduced the active length-tension behavior was shifted towards smaller stretches and a stronger contractile behavior at the low pressure domain together with a weaker contraction at the high pressure domain was observed.

Using the arterial ring model, the change of the average circumferential wall stress of the media was studied for different values of smooth muscle fiber orientation, and how the smooth muscle parameter N_{cu} and the filament overlap behavior could reverse this change at different pressures. The smooth muscle fibers were initially modeled to be oriented in the circumferential direction. It is assumed that the artery is in a homeostatic stress state. A change in the smooth muscle fiber orientation led to a weaker contractile behavior at all pressure domains compared to this healthy *in vivo* case and therefore to an increasing wall stress, as shown in Fig. 3.9. The stress increase was reversed by a 30% increase of the smooth muscle parameter N_{cu} or by modifying the filament overlap parameters (50% decrease of $\overline{\mathrm{u}}_{\mathrm{fs}}^{\mathrm{opt}}$ and a switch to a symmetric filament overlap behavior). At an internal pressure of 60 mmHg, the smooth muscle parameter N_{cu} and the filament overlap parame-

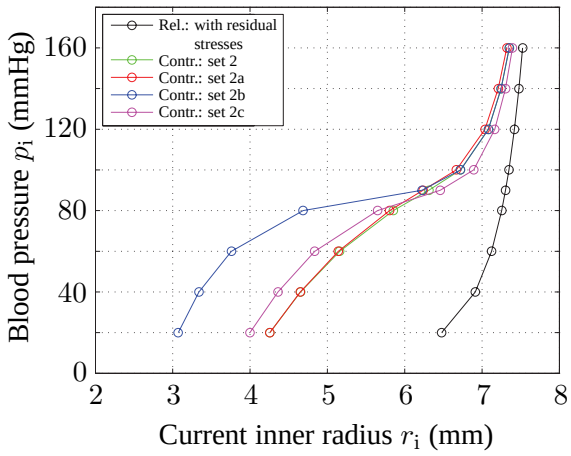

Figure 3.7 Influence of filament overlap parameters $\overline{\mathrm{u}}_{\mathrm{fs}}^{\mathrm{opt}}$, $\overline{\mathrm{s}}_{\mathrm{fo}_1}$ and $\overline{\mathrm{s}}_{\mathrm{fo}_2}$ on the pressure-radius relationship of the arterial ring.

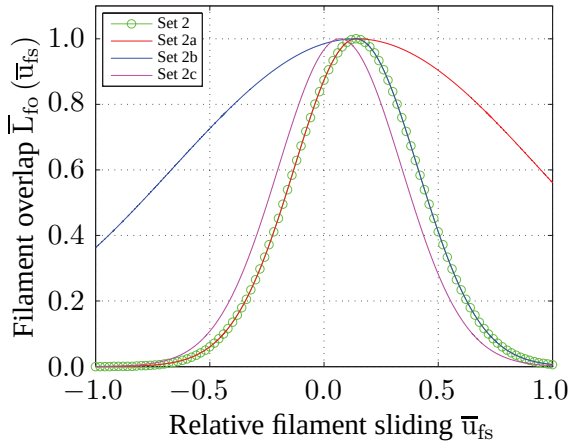

Figure 3.8 Filament overlap $\overline{\mathrm{L}}_{\mathrm{fo}}$ as a function of relative filament sliding $\overline{\mathrm{u}}_{\mathrm{fs}}$ for different sets of filament overlap parameters, corresponding to Fig. 3.7.

ter were able to reduce the increase in the wall stress. However, at 90 and 120 mmHg only the smooth muscle parameter N_{cu} was able to reduce the increase in the circumferential wall stress, see Fig. 3.9.

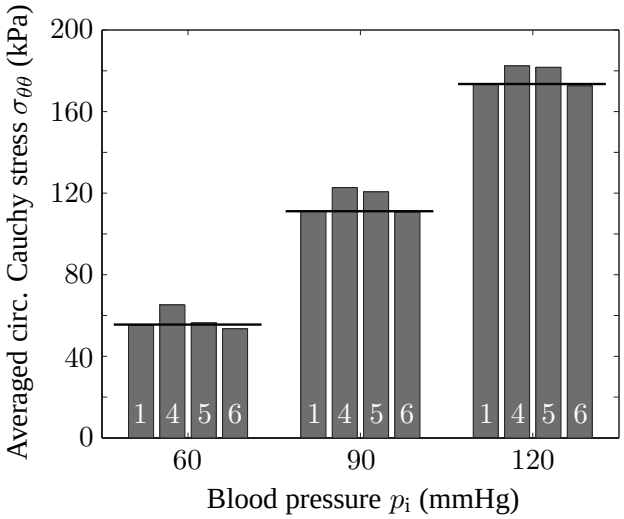

Figure 3.9 Effects of the interrelation between the extracellular smooth muscle orientation and the intra-cellular filament structure on the averaged circumferential Cauchy stress $\sigma_{\theta\theta}$ at three different blood pressure levels. Numbers inside the bars denote used material parameter sets, as defined in Table 3.4: (1) the healthy *in vivo* situation, (4) the reoriented smooth muscle fibers, (5) the decreased filament overlap parameter set ($\overline{\mathrm{u}}_{\mathrm{fs}}^{\mathrm{opt}}$, $\overline{\mathrm{s}}_{\mathrm{fo}_1}$, $\overline{\mathrm{s}}_{\mathrm{fo}_2}$), (6) the increased N_{cu}.

4. Discussion

In the present work we performed finite element analyses in order to study the quasi-static effects of smooth muscle remodeling, as reported in Gunst et al. (2003); Herrera et al. (2005); Syyong et al. (2008); Wang et al. (2001); Yamin and Morgan (2012) on the mechanical behavior of the human abdominal aorta. In particular, the influence of different smooth muscle fiber orientations, muscle contents (number of CUs) and different filament overlap behaviors on the pressure-radius relationship and the transmural stress distribution of the arterial wall was investigated. The recently proposed mechano-chemical constitutive model by Murtada et al. (2012) was modified in order to capture the mechanical behavior of two individual smooth muscle fiber families with a certain orientation and combined with a non-symmetric bell-shaped function in order to take the active length-tension behavior into account (Murtada et al., 2012). Active material parameters were obtained by fitting the model behavior to experimental data published by Murtada et al. (2012) and Niestrawska et al. (in press), for different smooth muscle fiber orientations. Due to the lack of available human active length-tension data sets, data from pig carotid arteries were scaled so as to represent the human active behavior. Fitting results highlighted trends for all active model parameters with respect to the smooth muscle orientation. Hence, an increasing α_{cu} led to monotonically increasing stiffness parameters (μ_{a} and κ_{AMp}) and monotonically decreasing filament overlap parameters ($\overline{\mathrm{u}}_{\mathrm{fs}}^{\mathrm{opt}}$, $\overline{\mathrm{s}}_{\mathrm{fo}_1}$ and $\overline{\mathrm{s}}_{\mathrm{fo}_2}$), because of decreasing muscle fiber stretches.

A non-symmetric filament overlap function was necessary for smooth muscle fibers aligned in the circumferential direction to capture the stretch-active stress behavior, suggesting a non-symmetry in the experimental stretch-active stress behavior. When fitting the model for different smooth muscle fiber orientations to the experimental stretch-active stress behavior, the non-symmetry in the filament overlap behavior decreased with increasing α_{cu}, and finally vanished for $\alpha_{\mathrm{cu}} = 30^{\circ}$ and above. We also found that simulations with higher values of α_{cu} undergo a larger rotation of the smooth muscle fibers for applied stretches in the circumferential direction than in simulations with smaller values of α_{cu}. These findings agree well with data presented by Chen et al. (2013), where they measured the current orientation of vascular smooth muscle cells as a function of the internal pressure. These results suggest that the non-symmetric behavior observed in the stretch-active stress behavior is more driven by the reorientation of smooth muscle fibers for $\alpha_{\mathrm{cu}} \geq 30^{\circ}$, and more driven by a non-symmetric filament overlap function for $\alpha_{\mathrm{cu}} \leq 30^{\circ}$. Based on the stretch-active stress behavior which we kept constant, a matching combination of smooth muscle fiber orientation and filament overlap behavior for best fit could be determined. Results suggest a symmetric-like filament overlap behavior and an optimal stretch value

closer to the resting stretch for smooth muscle fiber orientations deviating further away from the circumferential direction. Based on these results and the assumption that smooth muscle cells work close to its optimal stretch, vascular tissue with smooth muscle fiber orientation not aligned in the circumferential direction could be less pre-stretched. The active force produced by these smooth muscle cells would also behave more in a symmetric-like manner as a function of the applied stretch.

In the FE simulation of the medial strip, different smooth muscle fiber orientations were simulated. Medial strips with two symmetric muscle fibers with orientation of $\pm 30^{\circ}$ showed a significantly increased wall thickness compared to a medial strip with muscle fibers aligned in the circumferential direction as a result of the active contraction in the axial direction and the incompressibility condition. This illustrates the importance of the smooth muscle fiber orientation on the contractile response of the arterial tissue. There have been several reports of the existence of active stresses in both circumferential and axial directions in arteries indicating that smooth muscle contraction is responsible for a multiaxial response in the vascular wall (Agianniotis et al., 2012; Chen et al., 2013; Murtada et al., 2016a; Takamizawa et al., 1992). Structural investigations performed by Chen et al. (2013) and Holzapfel et al. (2002) also suggest that smooth muscle cells form two symmetric helically arranged fiber families in the artery with a orientation distribution similar to that of collagen fibers. A statistical orientation distribution of smooth muscle fibers has been addressed previously (Murtada et al., 2010b) but not using a FE implementation to study the three-dimensional effects of the orientation distribution.

The interrelation between extracellular smooth muscle fiber orientation and intracellular filament structure, and their influence on the human abdominal aorta was investigated using an analytical approach. By using the proposed model we have shown the influence of the smooth muscle fiber orientation on the mechanical integrity of the arterial wall. But also, how changes in the arterial wall behavior due to alteration in smooth muscle fiber orientation can be reduced, and even prevented by adjusting the filament overlap behavior or the smooth muscle contractile unit density. Thus, modifying the intracellular filament structure or the smooth muscle cell content could be used as a therapeutic approach in response to pathological vascular adaptation processes where changes in smooth muscle fiber orientation is involved. However, this would require further experimental and analytical studies.

Reports have suggested that an increase in smooth muscle cell content, here presented by an increase in numbers of CUs, is a part of a response due to vascular adaptation such as hypertension (Cox, 1981; Delbosc et al., 2008; Fridez et al., 2001; Zulliger et al., 2004). However, only a few studies have investigated if a coupled change in the smooth muscle orientation and intra-cellular structure occurred during this adaptive changes of the smooth muscle cells. Studying the orientation of smooth muscle cells during vascular adaptive processes could provide additional information and could also be used as a precursor for changes in smooth muscle cell content and intracellular changes in the myofilament structure.

In general, the incorporation of residual stresses in the abdominal aorta does not only

effect the pressure-radius relationship it also reduces the transmural stress gradients, a finding which is in agreement with, e.g., Holzapfel et al. (2000) and Humphrey (1995). The transmural circumferential stress distribution within the medial layer showed an almost horizontal line at the fully contracted state of smooth muscle cells compared to the relaxed state. Humphrey and Na (2002); Murtada and Holzapfel (2014) and Rachev and Hayashi (1999), for example, reported that a combination of residual stresses and basal smooth muscle contraction is responsible for a more homogeneous transmural stress distribution along the wall thickness, which also our results predict. Further, Humphrey and Na (2002) suggested that continuous adaptation processes of intramural constituents may seek to homogenize the stresses through the arterial wall thickness so that cells sense the same stress value independent of the radial location. That means, whenever loading conditions significantly alter, stress gradients change so that cells sense different stresses along the wall thickness, and remodeling mechanisms are triggered. Fung (1997) states that at homeostasis the strain energy, and hence the strain of every vascular smooth muscle cell is uniform, known as the principle of optimal operation. In contrast to our results, several studies which also considered residual stresses as well as vascular smooth muscle tone (Huo et al., 2013; Zulliger et al., 2004) predicted a positive stress gradient, i.e. an increase of the transmural stress from the inner to the outer surfaces at a physiological blood pressure level. However, in their models smooth muscle contraction also leads to a reduced averaged wall stress in the circumferential direction as well as a slightly reduced stress gradient compared to the fully relaxed state, which is in agreement with our results.

The presented results show that the proposed constitutive model is able to predict the expected mechanical behavior, in particular the stress distributions throughout the medial wall thickness, and it is therefore well suited for studying more complex physiological boundary-value problems in vascular mechanics. The presented results show that the proposed constitutive model is able to predict the expected mechanical behavior, in particular the stress distributions throughout the medial wall thickness, and is therefore well suited for studying more complex physiological boundary value problems in vascular mechanics. Furthermore, it allows a detailed quasi-static analysis of the effects of morphological and functional smooth muscle and collagen fiber alterations occurring during a disease development on the *in vivo* mechanical behavior of the human abdominal aorta, e.g., as seen in hypertension and abdominal aortic aneurysms. Nevertheless, exact triggering mechanisms of these diseases as well as corresponding complex correlations of alterations between active and passive constituents of the arterial wall with respect to the disease development are still objects of investigation.

Bibliography

A. Agianniotis, A. Rachev, and N. Stergiopulos. Active axial stress in mouse aorta. *J. Biomech.*, 45:1924–1927, 2012.

A. Arner. Mechanical characteristics of chemically skinned guinea-pig taenia coli. *Pflügers Arch.*, 395:277–284, 1982.

S. M. Arribas, J. F. Gordon, C. J. Daly, A. F. Dominiczak, and J. C. McGrath. Confocal microscopic characterization of a lesion in a cerebral vessel of the stroke-prone spontaneously hypertensive rat. *Stroke*, 27:1118–1123, 1996.

J. T. Butcher and R. M. Nerem. Valvular endothelial cells and the mechanoregulation of valvular pathology. *Philos. Trans. R. Soc. B Biol. Sci.*, 362:1445–1457, 2007.

B. E. Carlson and T. W. Secomb. A theoretical model for the myogenic response based on the length-tension characteristics of vascular smooth muscle. *Microcirculation*, 12: 327–338, 2005.

H. Chen, T. Luo, X. Zhao, X. Lu, Y. Huo, and G. S. Kassab. Microstructural constitutive model of active coronary media. *Biomaterials*, 34:7575–7583, 2013.

Q. Chen, W. Li, Z. Quan, and B. E. Sumpio. Modulation of vascular smooth muscle cell alignment by cyclic strain is dependent on reactive oxygen species and P38 mitogen-activated protein kinase. *J. Vasc. Surg.*, 37:660–668, 2003.

R. H. Cox. Arterial wall mechanics and composition and the effects of smooth muscle activation. *Am. J. Physiol.*, 229:807–812, 1975.

R. H. Cox. Regional variation of series elasticity in canine arterial smooth muscles. *Am. J. Physiol.*, 234:H542–H551, 1978.

R. H. Cox. Basis for the altered arterial wall mechanics in the spontaneously hypertensive rat. *Hypertension*, 3:485–495, 1981.

S. Delbosc, M. Haloui, L. Louedec, M. Dupuis, M. Cubizolles, V. N. Podust, E. T. Fung, J. B. Michel, and O. Meilhac. Proteomic analysis permits the identification of new biomarkers of arterial wall remodeling in hypertension. *Mol. Med.*, 14:383–394, 2008.

P. B. Dobrin. Influence of initial length on length-tension relationship of vascular smooth muscle. *Am. J. Physiol.*, 225:664–670, 1973.

J. Ferruzzi, M. R. Bersi, S. Uman, H. Yanagisawa, and J. D. Humphrey. Decreased elastic energy storage, not increased material stiffness, characterizes central artery dysfunction in fibulin-5 deficiency independent of sex. *J. Biomech. Eng.*, 137:31007, 2015.

P. J. Flory. Thermodynamic relations for high elastic materials. *Trans. Faraday Soc.*, 57: 829–838, 1961.

P. Fridez, A. Makino, H. Miyazaki, J. J. Meister, K. Hayashi, and N. Stergiopulos. Short-term biomechanical adaptation of the rat carotid to acute hypertension: contribution of smooth muscle. *Ann. Biomed. Eng.*, 29:26–34, 2001.

Y.-C. Fung. *Biomechanics: Circulation*. Springer-Verlag, New York, 2nd edition, 1997.

R. L. Gleason, W. W. Dye, E. Wilson, and J. D. Humphrey. Quantification of the mechanical behavior of carotid arteries from wild-type, dystrophin-deficient, and sarcoglycan-delta knockout mice. *J. Biomech.*, 41:3213–3218, 2008.

W. H. Guilford and D. M. Warshaw. The molecular mechanics of smooth muscle myosin. *Comp. Biochem. Physiol. B Biochem. Mol. Biol.*, 119:451–458, 1998.

S. J. Gunst, D. D. Tang, and A. Opazo Saez. Cytoskeletal remodeling of the airway smooth muscle cell: A mechanism for adaptation to mechanical forces in the lung. *Respir. Physiol. Neurobiol.*, 137:151–168, 2003.

C. M. Hai and R. A. Murphy. Cross-bridge phosphorylation and regulation of latch state in smooth muscle. *Am. J. Physiol.*, 254:C99–106, 1988.

A. M. Herrera, B. E. McParland, A. Bienkowska, R. Tait, P. D. Paré, and C. Y. Seow. 'Sarcomeres' of smooth muscle: functional characteristics and ultrastructural evidence. *J. Cell Sci.*, 118:2381–2392, 2005.

A. V. Hill. The heat of shortening and the dynamic constants of muscle. *Proc. R. Soc. B Biol. Sci.*, 126:136–195, 1938.

G. A. Holzapfel. *Nonlinear Solid Mechanics: A Continuum Approach for Engineering*. John Wiley & Sons, Chichester, 2000.

G. A. Holzapfel and R. W. Ogden. Modelling the layer-specific three-dimensional residual stresses in arteries, with an application to the human aorta. *J. R. Soc. Interface*, 7:787–799, 2010.

G. A. Holzapfel, T. C. Gasser, and R. W. Ogden. A new constitutive framework for arterial wall mechanics and a comparative study of material models. *J. Elast.*, 61:1–48, 2000.

G. A. Holzapfel, T. C. Gasser, and M. Stadler. A structural model for the viscoelastic behavior of arterial walls: Continuum formulation and finite element analysis. *Eur. J. Mech. A/Solids*, 21:441–463, 2002.

G. A. Holzapfel, G. Sommer, M. Auer, P. Regitnig, and R. W. Ogden. Layer-specific 3D residual deformations of human aortas with non-atherosclerotic intimal thickening. *Ann. Biomed. Eng.*, 35:530–545, 2007.

G. A. Holzapfel, J. A. Niestrawska, R. W. Ogden, A. J. Reinisch, and A. J. Schriefl. Modelling non-symmetric collagen fibre dispersion in arterial walls. *J. R. Soc. Interface*, 3: 15–35, 2015.

L. Horný, J. Kronek, H. Chlup, R. Zitny, J. Vesely, and M. Hulan. Orientations of collagen fibers in aortic histological section. *Bull. Appl. Mech.*, 6:25–29, 2010.

L. Horný, M. Netušil, and T. Voavková. Axial prestretch and circumferential distensibility in biomechanics of abdominal aorta. *Biomech. Model. Mechanobiol.*, 13:783–799, 2014.

J. D. Humphrey. Mechanics of the arterial wall: review and directions. *Crit. Rev. Biomed. Eng.*, 23:1–162, 1995.

J. D. Humphrey. *Cardiovascular Solid Mechanics: Cells, tissues and organs*. Springer-Verlag, New York, 2002.

J. D. Humphrey and S. Na. Elastodynamics and arterial wall stress. *Ann. Biomed. Eng.*, 30:509–523, 2002.

Y. Huo, X. Zhao, Y. Cheng, X. Lu, and G. S. Kassab. Two-layer model of coronary artery vasoactivity. *J. Appl. Physiol.*, 114:1451–1459, 2013.

M. R. Labrosse, C. J. Beller, T. Mesana, and J. P. Veinot. Mechanical behavior of human aortas: Experiments, material constants and 3-D finite element modeling including residual stress. *J. Biomech.*, 42:996–1004, 2009.

Q. Li, Y. Muragaki, I. Hatamura, H. Ueno, and A. Ooshima. Stretch-induced collagen synthesis in cultured smooth muscle cells from rabbit aortic media and a possible involvement of angiotensin II and transforming growth factor-beta. *J. Vasc. Res.*, 35:93–103, 1998.

B. Liu, M. J. Qu, K. R. Qin, H. Li, Z. K. Li, B. R. Shen, and Z. L. Jiang. Role of cyclic strain frequency in regulating the alignment of vascular smooth muscle cells in vitro. *Biophys. J.*, 94:1497–1507, 2008.

L. E. Mantella, A. Quan, and S. Verma. Variability in vascular smooth muscle cell stretch-induced responses in 2D culture. *Vasc. Cell*, 7:7, 2015.

S. Murtada and G. A. Holzapfel. Investigating the role of smooth muscle cells in large elastic arteries: A finite element analysis. *J. Theor. Biol.*, 358:1–10, 2014.

S. Murtada, M. Kroon, and G. A. Holzapfel. A calcium-driven mechanochemical model for prediction of force generation in smooth muscle. *Biomech. Model. Mechanobiol.*, 9: 749–762, 2010a.

S. Murtada, M. Kroon, and G. A. Holzapfel. Modeling the dispersion effects of contractile fibers in smooth muscles. *J. Mech. Phys. Solids*, 58:2065–2082, 2010b.

S. Murtada, A. Arner, and G. A. Holzapfel. Experiments and mechanochemical modeling of smooth muscle contraction: Significance of filament overlap. *J. Theor. Biol.*, 297: 176–186, 2012.

S. Murtada, J. Ferruzzi, H. Yanagisawa, and J. D. Humphrey. Reduced biaxial contractility in the descending thoracic aorta of fibulin-5 deficient mice. *J. Biomech. Eng.*, 138:51008, 2016a.

S. Murtada, S. Lewin, A. Arner, and J. D. Humphrey. Adaptation of active tone in the mouse descending thoracic aorta under acute changes in loading. *Biomech. Model. Mechanobiol.*, 15:579–592, 2016b.

J. Niestrawska, C. Viertler, P. Regitnig, T. Cohnert, G. Sommer, and G. A. Holzapfel. Microstructure and mechanics of healthy and aneurysmatic abdominal aortas: experimental analysis and modeling. *J. R. Soc. Interface*, in press.

R. W. Ogden. Nearly isochoric elastic deformations: Application to rubberlike solids. *J. Mech. Phys. Solids*, 26:37–57, 1978.

R. W. Ogden. *Non-linear Elastic Deformations*. Dover, New York, 1997.

A. Rachev and K. Hayashi. Theoretical study of the effects of vascular smooth muscle contraction on strain and stress distributions in arteries. *Ann. Biomed. Eng.*, 27:459–468, 1999.

J. Stålhand, A. Klarbring, and G. A. Holzapfel. A mechanochemical 3D continuum model for smooth muscle contraction under finite strains. *J. Theor. Biol.*, 268:120–130, 2011.

P. R. Standley, A. Cammarata, B. P. Nolan, C. T. Purgason, M. A. Stanley, and A. Camaratta. Cyclic stretch induces vascular smooth muscle cell alignment via NO signaling. *Am. J. Physiol. Heart Circ. Physiol.*, 283:H1907–H1914, 2002.

H. Syyong, C. Cheung, D. Solomon, C. Y. Seow, and K. H. Kuo. Adaptive response of pulmonary arterial smooth muscle to length change. *J. Appl. Physiol.*, 104:1014–1020, 2008.

K. Takamizawa, K. Hayashi, and T. Matsuda. Isometric biaxial tension of smooth muscle in isolated cylindrical segments of rabbit arteries. *Am. J. Physiol.*, 263:H30–H34, 1992.

R. L. Taylor. *FEAP – A Finite Element Analysis Program, Version 8.4 User Manual*. University of California at Berkeley, Berkeley, California, 2013.

L. Wang, P. D. Paré, and C. Y. Seow. Selected contribution: effect of chronic passive length change on airway smooth muscle length-tension relationship. *J. Appl. Physiol.*, 90:734–740, 2001.

P. Wriggers. *Nonlinear Finite Element Methods*. Springer-Verlag, Berlin, Heidelberg, 2008.

R. Yamin and K. G. Morgan. Deciphering actin cytoskeletal function in the contractile vascular smooth muscle cell. *J. Physiol.*, 590:4145–4154, 2012.

O. C. Zienkiewicz and R. L. Taylor. *The Finite Element Method. The Basis*, volume 1. Butterworth Heinemann, Oxford, 5th edition, 2000.

M. A. Zulliger, A. Rachev, and N. Stergiopulos. A constitutive formulation of arterial mechanics including vascular smooth muscle tone. *Am. J. Physiol. Heart Circ. Physiol.*, 287:H1335–H1343, 2004.

Appendices

A. Detailed Derivation of the Stress and Elasticity Tensors

The purely volumetric stress contribution $\mathbf{S}_{\mathrm{vol}}$ is specified by Eq. (2.7), where the derivative of J with respect to the symmetric tensor $\mathbf{C}$ is

$$\frac{\partial J}{\partial \mathbf{C}} = \frac{\partial}{\partial I_3}\left(I_3^{1/2}\right)\frac{\partial I_3}{\partial \mathbf{C}} = \frac{1}{2}I_3^{-1/2}I_3\mathbf{C}^{-1} = \frac{1}{2}I_3^{1/2}\mathbf{C}^{-1} = \frac{1}{2}J\mathbf{C}^{-1}, \tag{A.1}$$

where we have used Eq. (2.4).

In order to derive the isochoric stress tensor $\overline{\mathbf{S}}$, as shown in Eq. (2.8), it is necessary to introduce the derivative of the modified right Cauchy-Green tensor $\overline{\mathbf{C}}$ relative to the symmetric tensor $\mathbf{C}$, in which we use the fourth-order projection tensor $\mathbb{P}$ in the reference configuration. Thus, the projection tensor $\mathbb{P}$ and its properties are

$$\begin{aligned}\mathbb{P} &= \mathbb{I} - \frac{1}{3}\mathbf{C}^{-1}\otimes\mathbf{C} = \mathbb{I} - \frac{1}{3}\left(\mathbf{C}\otimes\mathbf{C}^{-1}\right)^{\mathrm{T}} \\ &= \mathbb{I} - \frac{1}{3}\overline{\mathbf{C}}^{-1}\otimes\overline{\mathbf{C}} = \mathbb{I} - \frac{1}{3}\left(\overline{\mathbf{C}}\otimes\overline{\mathbf{C}}^{-1}\right)^{\mathrm{T}},\end{aligned} \tag{A.2}$$

together with the fourth-order identity tensor

$$\left(\mathbb{I}\right)_{\mathrm{ABCD}} = \left(\delta_{AC}\delta_{BD} + \delta_{AD}\delta_{BC}\right)/2, \tag{A.3}$$

where $\delta_{AC}, \delta_{BD}, \delta_{AD}$ and δ_{BC} denote the Kronecker delta. By means of Eqs. (A.1)-(A.3), the standard result of the derivative of $\overline{\mathbf{C}}$ with respect to $\mathbf{C}$ is

$$\begin{aligned}\frac{\partial\overline{\mathbf{C}}}{\partial\mathbf{C}} &= \frac{\partial\left(J^{-2/3}\mathbf{C}\right)}{\partial\mathbf{C}} = J^{-2/3}\frac{\partial\mathbf{C}}{\partial\mathbf{C}} + \mathbf{C}\otimes\frac{\partial J^{-2/3}}{\partial\mathbf{C}} \\ &= J^{-2/3}\mathbb{I} + \mathbf{C}\otimes\frac{\partial J^{-2/3}}{\partial J}\frac{\partial J}{\partial\mathbf{C}} = J^{-2/3}\left(\mathbb{I} - \frac{1}{3}\mathbf{C}\otimes\mathbf{C}^{-1}\right) \\ &= J^{-2/3}\mathbb{P}^{\mathrm{T}},\end{aligned} \tag{A.4}$$

in which $\mathbb{P}^{\mathrm{T}}$ defines the transpose of the fourth-order tensor $\mathbb{P}$. With the use of Eqs. (A.1)-(A.4), the purely isochoric stress contribution can be derived as

$$\begin{aligned}\overline{\mathbf{S}} &= 2\frac{\partial\overline{\Psi}(\overline{\mathbf{C}})}{\partial\mathbf{C}} = 2\frac{\partial\overline{\Psi}(\overline{\mathbf{C}})}{\partial\overline{\mathbf{C}}} : \frac{\partial\overline{\mathbf{C}}}{\partial\mathbf{C}} = 2\frac{\partial\overline{\Psi}(\overline{\mathbf{C}})}{\partial\overline{\mathbf{C}}} : J^{-2/3}\mathbb{P}^{\mathrm{T}} = J^{-2/3}\mathbb{P} : 2\frac{\partial\overline{\Psi}(\overline{\mathbf{C}})}{\partial\overline{\mathbf{C}}} \\ &= J^{-2/3}\left[2\frac{\partial\overline{\Psi}(\overline{\mathbf{C}})}{\partial\overline{\mathbf{C}}} - \frac{1}{3}\left(\overline{\mathbf{C}} : 2\frac{\partial\overline{\Psi}(\overline{\mathbf{C}})}{\partial\overline{\mathbf{C}}}\right)\overline{\mathbf{C}}^{-1}\right].\end{aligned} \tag{A.5}$$

Finally, by introducing the deviatoric operator in the Lagrangian description, defined as

$$\mathrm{Dev}\left[\bullet\right] = (\bullet) - \frac{1}{3}\left[(\bullet) : \overline{\mathbf{C}}\right]\overline{\mathbf{C}}^{-1} = (\bullet) - \frac{1}{3}\left[\overline{\mathbf{C}} : (\bullet)\right]\overline{\mathbf{C}}^{-1} = \mathbb{P} : (\bullet) = (\bullet) : \mathbb{P}^{\mathrm{T}}, \quad \text{(A.6)}$$

a rather convenient short-hand notation can be used for the isochoric contribution of the second Piola-Kirchhoff stress, as shown in Eq. (2.8).

The purely volumetric contribution of the elasticity tensor in the Lagrangian description of Eq. (2.12) can be derivated as

$$\begin{aligned}\mathbb{C}_{\mathrm{vol}} &= 2\left(\mathbf{C}^{-1} \otimes \frac{\partial\left(pJ\right)}{\partial\mathbf{C}} + pJ\frac{\partial\mathbf{C}^{-1}}{\partial\mathbf{C}}\right)\\ &= 2\mathbf{C}^{-1} \otimes \left(p + J\frac{\mathrm{d}p}{\mathrm{d}J}\right)\frac{\partial J}{\partial\mathbf{C}} - 2pJ\mathbf{C}^{-1} \odot \mathbf{C}^{-1},\end{aligned} \quad \text{(A.7)}$$

where the definition for the fourth-order tensor

$$\begin{aligned}\left(\frac{\partial\mathbf{C}^{-1}}{\partial\mathbf{C}}\right)_{ABCD} &= -\left(\mathbf{C}^{-1} \odot \mathbf{C}^{-1}\right)_{ABCD}\\ &= -\frac{1}{2}\left(C^{-1}_{AC}C^{-1}_{BD} + C^{-1}_{AD}C^{-1}_{BC}\right) = \frac{\partial C^{-1}_{AB}}{\partial C_{CD}}\end{aligned} \quad \text{(A.8)}$$

has been used.

B. Analytical Expressions for Fitting

As already mentioned the proposed active model is fitted to modified experimental data obtained from uniaxial isometric contraction tests performed on circumferential strips which are cut out from the dissected medial layer. Hence, analytical expressions are presented which are required for the subsequent fitting procedure. Therefore, the purely incompressible formulation of a hyperelastic material is considered where the free-energy function Ψ for the medial layer is characterized by $\Psi = \Psi_{\mathrm{a}} + \Psi_{\mathrm{p}}$, with the active contribution according to Eq. (2.25) (without bars on the variables) and the passive contribution according to Eqs. (2.36)-(2.40) (again without bars on the variables). The incompressible formulation of the analytical expression for the second Piola-Kirchhoff stress tensor **S** then reads

$$\begin{aligned}\mathbf{S} &= 2\frac{\partial \Psi}{\partial \mathbf{C}} - p\mathbf{C}^{-1} \\ &= 2\left\{\Psi_{\mathrm{p}}'\left(I_1\right)\mathbf{I} + \sum_{i=4,\,6}\left[\Psi_{\mathrm{p}}'\left(I_{\mathrm{fib}_i}^{\star}\right)\mathbf{H}_i + \Psi_{\mathrm{a}}'\left(I_{\mathrm{cu}_i}\right)\mathbf{M}_{\mathrm{cu}_i}\otimes\mathbf{M}_{\mathrm{cu}_i}\right]\right\} - p\mathbf{C}^{-1}, \quad \text{(B.1)}\end{aligned}$$

where p is a Lagrange multiplier to enforce incompressibility. The Cauchy stress tensor $\boldsymbol{\sigma}$ can then be computed by $\boldsymbol{\sigma} = \mathbf{FSF}^{\mathrm{T}}$.

We consider now a circumferential specimen (medial layer) with two symmetric fiber families and with mean fiber directions in the reference configuration denoted by

$$\left[\mathbf{M}_{\mathrm{fib}_4}\right] = \left[0,\,\cos\alpha_{\mathrm{fib}},\,\sin\alpha_{\mathrm{fib}}\right]^{\mathrm{T}},\left[\mathbf{M}_{\mathrm{fib}_6}\right] = \left[0,\,\cos\alpha_{\mathrm{fib}},\,-\sin\alpha_{\mathrm{fib}}\right]^{\mathrm{T}}, \qquad \text{(B.2)}$$

while the normal direction to the circumferential/axial plane coincides with the radial direction vector $\mathbf{e}_r$ given by $\left[\mathbf{M}_{\mathrm{n}}\right] = \left[1,\,0,\,0\right]^{\mathrm{T}}$, see Fig. 2.1. Further, two symmetric smooth muscle fiber families are oriented along the direction vectors and characterized by

$$\left[\mathbf{M}_{\mathrm{cu}_4}\right] = \left[0,\,\cos\alpha_{\mathrm{cu}},\,\sin\alpha_{\mathrm{cu}}\right]^{\mathrm{T}},\left[\mathbf{M}_{\mathrm{cu}_6}\right] = \left[0,\,\cos\alpha_{\mathrm{cu}},\,-\sin\alpha_{\mathrm{cu}}\right]^{\mathrm{T}}, \qquad \text{(B.3)}$$

defined in the reference configuration, see also Fig. 2.1. Note that the angles α_{fib} and α_{cu} are always measured with respect to the circumferential direction. The corresponding deformation gradient **F** for uniaxial extension or compression as well as the right and left Cauchy-Green tensors $(\mathbf{C}, \mathbf{b})$ can be expressed in terms of the principal stretches by (shear is neglected)

$$\left[\mathbf{F}\right] = \mathrm{diag}\left[\lambda_r,\,\lambda_\theta,\,\lambda_z\right],\left[\mathbf{C}\right] = \mathrm{diag}\left[\lambda_r^2,\,\lambda_\theta^2,\,\lambda_z^2\right] = \left[\mathbf{b}\right]. \qquad \text{(B.4)}$$

The required invariants are also expressed in terms of principal stretches, and read

$$I_1 = \lambda_r^2 + \lambda_\theta^2 + \lambda_z^2, \quad I_\mathrm{n} = \mathbf{C} : \mathbf{M}_\mathrm{n} \otimes \mathbf{M}_\mathrm{n} = \lambda_r^2, \tag{B.5}$$

$$I_{\mathrm{fib}_i} = \mathbf{C} : \mathbf{M}_{\mathrm{fib}_i} \otimes \mathbf{M}_{\mathrm{fib}_i} = \lambda_\theta^2 \cos^2 \alpha_\mathrm{fib} + \lambda_z^2 \sin^2 \alpha_\mathrm{fib}, \tag{B.6}$$

$$I_{\mathrm{cu}_i} = \mathbf{C} : \mathbf{M}_{\mathrm{cu}_i} \otimes \mathbf{M}_{\mathrm{cu}_i} = \lambda_\theta^2 \cos^2 \alpha_\mathrm{cu} + \lambda_z^2 \sin^2 \alpha_\mathrm{cu}, \tag{B.7}$$

with $i = 4,\ 6$. The derivatives of the free-energy functions relative to the defined invariants necessary for Eq. (B.1) are then given by

$$\Psi'_\mathrm{a}\left(I_{\mathrm{cu}_i}\right) = \frac{\partial \Psi_\mathrm{a}}{\partial I_{\mathrm{cu}_i}} = \frac{\mu_\mathrm{a} \overline{\mathrm{L}}_{\mathrm{fo}_i}}{2} \left(n_\mathrm{AMp} + n_\mathrm{AM}\right) \frac{\sqrt{I_{\mathrm{cu}_i}} - \overline{\mathrm{u}}_{\mathrm{fs}_i} - 1}{\sqrt{I_{\mathrm{cu}_i}}}, \qquad i = 4, 6, \tag{B.8}$$

$$\Psi'_\mathrm{p}\left(I_1\right) = \frac{\partial \Psi_\mathrm{p}}{\partial I_1} = \frac{\mu_\mathrm{p}}{2}, \tag{B.9}$$

$$\Psi'_\mathrm{p}\left(I^\star_{\mathrm{fib}_i}\right) = \frac{\partial \Psi_\mathrm{p}}{\partial I^\star_{\mathrm{fib}_i}} = C_1 \ \left(I^\star_{\mathrm{fib}_i} - 1\right) \exp\left[C_2 \left(I^\star_{\mathrm{fib}_i} - 1\right)^2\right], \qquad i = 4, 6. \tag{B.10}$$

Hence, the non-zero components of the Cauchy stress matrix $[\boldsymbol{\sigma}]$ read

$$\sigma_{rr} = -p + 2 \left[\Psi'_\mathrm{p}\left(I_1\right) + \sum_{i=4,\ 6} \left(1 - 2A - B\right) \Psi'_\mathrm{p}\left(I^\star_{\mathrm{fib}_i}\right)\right] \lambda_r^2, \tag{B.11}$$

$$\begin{aligned}\sigma_{\theta\theta} = -p + 2 \Bigg[&\Psi'_\mathrm{p}\left(I_1\right) + \sum_{i=4,\ 6} \left(A + B \cos^2 \alpha_\mathrm{fib}\right) \Psi'_\mathrm{p}\left(I^\star_{\mathrm{fib}_i}\right) \\ &+ \sum_{i=4,\ 6} \Psi'_\mathrm{a}\left(I_{\mathrm{cu}_i}\right) \cos^2 \alpha_\mathrm{cu}\Bigg] \lambda_\theta^2,\end{aligned} \tag{B.12}$$

$$\begin{aligned}\sigma_{zz} = -p + 2 \Bigg[&\Psi'_\mathrm{p}\left(I_1\right) + \sum_{i=4,\ 6} \left(A + B \sin^2 \alpha_\mathrm{fib}\right) \Psi'_\mathrm{p}\left(I^\star_{\mathrm{fib}_i}\right) \\ &+ \sum_{i=4,\ 6} \Psi'_\mathrm{a}\left(I_{\mathrm{cu}_i}\right) \sin^2 \alpha_\mathrm{cu}\Bigg] \lambda_z^2.\end{aligned} \tag{B.13}$$

By solving this system of equations, so that the boundary condition $\sigma_{rr} = \sigma_{zz} = 0$ and the incompressibility condition $J = 1 = \lambda_r \lambda_\theta \lambda_z$ are satisfied, the normal stress in the circumferential direction of the tested medial specimen $\sigma_{\theta\theta}$ can be expressed as a function of the principal stretch in the circumferential direction λ_θ. The first Piola-Kirchhoff stress $\mathrm{P}_{\theta\theta}$ can then be calculated from $\mathrm{P}_{\theta\theta} = \sigma_{\theta\theta} / \lambda_\theta$.

C. Experimental Data Scaling

According to Murtada et al. (2012) we assume that the maximum contractility is expected to be within the physiological blood pressure range, i.e. around 90 mmHg. Numerical investigations (see arterial ring example) indicated a circumferential stretch of 1.28 at the inner radius of a healthy abdominal aorta under an internal pressure of 90 mmHg and an axial pre-stretch of 1.0675 (Horný et al., 2014) without considering smooth muscle contraction. This result is in good agreement with experimental data presented in Labrosse et al. (2009). Thus, the original length-tension behavior is scaled in the horizontal direction so that the maximum is situated at this obtained circumferential stretch. Further, it is assumed that the ratio between the active stress peak and the corresponding passive stress is the same for both pig carotid artery and human abdominal aorta, and therefore the experimental length-tension behavior is scaled in the vertical direction accordingly, see Fig. 3.1(a). Moreover, we also scale the corresponding active tension-time behavior, as shown in Murtada et al. (2012), according to the latter assumption. Both, modified length-tension and tension-time data of a medial strip are used for the parameter identification.